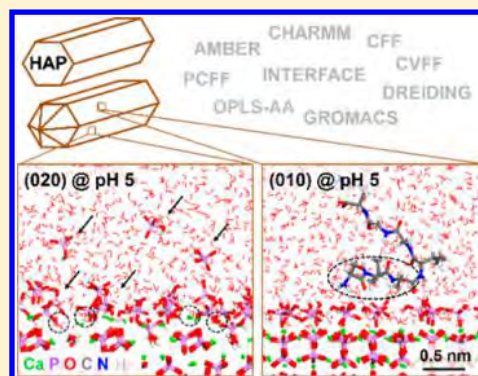


Accurate Force Field Parameters and pH Resolved Surface Models for Hydroxyapatite to Understand Structure, Mechanics, Hydration, and Biological Interfaces

Tzu-Jen Lin[†] and Hendrik Heinz^{*,†,‡}[†]Department of Polymer Engineering, University of Akron, Akron, Ohio 44325, United States[‡]Department of Chemical and Biological Engineering, University of Colorado at Boulder, Boulder, Colorado 80309, United States

Supporting Information

ABSTRACT: Mineralization of bone and teeth involves interactions between biomolecules and hydroxyapatite. Associated complex interfaces and processes remain difficult to analyze at the 1 to 100 nm scale using current laboratory techniques, and prior apatite models for atomistic simulations have been limited in the representation of chemical bonding, surface chemistry, and interfacial interactions. In this contribution, an accurate force field along with pH-resolved surface models for hydroxyapatite is introduced to represent chemical bonding, structural, surface, interfacial, and mechanical properties in quantitative agreement with experiment. The accuracy is orders of magnitude higher in comparison to earlier models and facilitates quantitative monitoring of inorganic-biological assembly. The force field is integrated into the AMBER, CHARMM, CFF, CVFF, DREIDING, GROMACS, INTERFACE, OPLS-AA, and PCFF force fields to enable realistic simulations of apatite-biological systems of any composition and ionic strength. Specific properties that are reproduced well in comparison to experiment include lattice constants (<0.5% deviation), IR spectrum, cleavage energies, immersion energies in water (<5% deviation), and elastic constants (<10% deviation). Interactions between mineral, water, and organic compounds are represented by standard combination rules without additional adjustable parameters and shown to achieve quantitative precision. Surface models for common (001), (010), (020), and (101) facets and nanocrystals are introduced as a function of pH on the basis of extensive experimental data. New insights into surface and immersion energies, the structure of aqueous interfaces, density profiles, and superficial dissolution are described. Most notably, hydroxyapatite-water interfaces exhibit facet-specific and pH-specific density profiles. Water stabilizes (010) facets better than (001) facets in a pH range from 10 to 5, consistent with preferred nanocrystal shape and growth in the (001) direction observed in experiment. Towards lower pH values, increasing penetration of water into sub-surface layers is observed, water density profiles flatten, and superficial dissolution occurs. The force field and surface models can be applied to elucidate mechanisms of mineralization as well as specific binding and assembly of peptides, polymer, and drugs. Extensions to substituted and defective apatites as well as to other calcium phosphate phases are feasible.



1. INTRODUCTION

Hydroxyapatite (HAP), $\text{Ca}_{10}(\text{PO}_4)_6(\text{OH})_2$, is the major mineral phase in human bone and teeth embedded in a matrix of collagen and other biomolecules.^{1–14} Substitutions such as partial replacement of calcium ions by magnesium ions, hydroxide ions by fluoride ions, or phosphate groups by carbonate groups are common and lead to variable compositions. Apatites and related calcium minerals are of great importance for human health due to the presence in bone and teeth, as well as their role in maladies such as osteoporosis, caries and coronary calcification that affect the quality of life of billions of people.^{1,2,7,11,13,15–33} Better understanding and engineering of the complex surface chemistry and assembly of apatite nanostructures embedded in biological environments from the atomic to microstructural scale could therefore facilitate major discoveries. Current experimental methods,

laboratory tests, and clinical studies cannot easily visualize or thermodynamically analyze related processes at the 1 to 100 nm scale and could greatly benefit from complementary molecular simulations.³⁴

Biom mineralization usually involves biopolymers and small molecules which control the spatial orientation and pattern of crystal growth in a cell, the composition and type of mineral phases, as well as the development of facets, shape, and crystallite size.^{1–3} Specific interactions between apatite surfaces and proteins are known to involve electrostatics (ion pairing),^{35–39} hydrogen bonds, hydrophobic interactions, and conformation effects.^{37,39} The fundamental mechanisms of

Received: December 21, 2015

Revised: February 12, 2016

Published: February 16, 2016

recognition are similar to those known for biomolecule adsorption on other oxidic surfaces with comparable density of ionic groups per unit area such as silica and cement minerals.^{40–44} The elucidation of the relative importance of interactions and mineralization mechanisms has yet remained an enigma since quantitative data from experimental measurements are limited, adequate simulation tools were not available, and the phase space of possible environments and structures has virtually no limits even at the nanometer scale. Specific recognition and crystallization properties of apatites are likely associated with the distinctive surface structure and surface chemistry of apatites as a function of crystallographic facets, facet size,⁴⁵ defects, as well as changes in pH and other solution conditions.⁴⁰

Details of the structure and composition of hydroxyapatite surfaces have been obtained in experiment by solubility measurements, acid-base titrations, adsorption isotherms, IR, NMR, AFM, SEM, TEM, XPS, as well as Auger electron spectroscopy studies, and these observations indicate notable differences to the structure of the bulk mineral.^{46–62} At the same time, uncertainties remain in experiment related to the use of polycrystalline samples versus single crystals, well-defined even surfaces versus imperfect hydrated surfaces, the type of displayed facets, defects, and specific details on biomolecular adsorption. For example, some reports indicate that peptides with a high proportion of glutamic and aspartic acids favor adsorption; yet other reports highlight the attraction of peptides with few or no acidic amino acid groups to apatite-based materials.^{19,30,32,37,63–65} Studies using phage display found that the peptide sequences SVSVGMPKSPRP and SVSVGK have a high affinity to HAP surfaces.^{31,66} Recent simulations have shown that the attraction of the amino acid motif SVSV to the hydroxyapatite prismatic plane is strongly pH dependent with significant adsorption at pH values found in bone (pH ~5) while a different set of ionic residues preferentially adsorbs at higher pH values (pH ~10), beginning to clarify experimental results.^{40,67}

Reliable force fields and surface models for apatites will eventually reveal contributions of different binding mechanisms of biomolecules to HAP surfaces and nanostructures, as seen for other nanostructures,^{40,42,43,45,68–73} thereby advancing the understanding of crystal growth and dissolution. As an ultimate goal, molecular-level signatures of diseases such as osteoporosis, caries, and artery calcification might be better understood to support preventive care and medical treatments. This contribution is a first step in this direction, introducing an accurate force field and a suite of chemically realistic surface models for hydroxyapatite. The proposed model takes into account the chemistry and stoichiometry of hydroxyapatite, offers an interpretation of all force field parameters, and reproduces bulk and surface properties quantitatively (including structures and energies). Facet-specific as well as pH-specific interactions with water will be explained, and follow-on contributions will explain selective interactions with peptides and drug molecules.⁶⁷ The hydroxyapatite model is integrated into the INTERFACE force field, fully compatible with a range of other energy expressions (CHARMM, AMBER, OPLS-AA, DREIDING, GROMACS, CVFF, and PCFF), and easily extensible for alternate stoichiometry using parameters for other ions and compounds.⁷⁴

The outline is as follows. In section 2, limitations of prior models and new capabilities are described. Results and discussions follow in sections 3 to 7. The force field parameters

are introduced in section 3. The surface models of hydroxyapatite including different facets and pH conditions are described in section 4. Evaluation of bulk properties is described in section 5, surface properties upon cleavage in section 6, and properties of aqueous hydroxyapatite interfaces in section 7. Section 7 also includes an example of facet and pH-dependent peptide adsorption. Conclusions are presented in section 8. Complete details of methods including simulation protocols, detailed descriptions of the force field derivation, and validation are given in the Supporting Information. This work may also serve as a resource for a broad range of experimental data for apatites, which have been used to validate the models in sections 3–7.

2. PRIOR STATE-OF-THE-ART AND NEW DEVELOPMENTS

Simulation methods at length scales from 0.1 to 1000 nm include ab initio molecular dynamics, hybrid methods such as QM/MM, classical atomistic molecular dynamics (MD), as well as coarse grain and continuum methods.⁷⁴ Classical all-atom molecular dynamics methods use chemically realistic models and reach length scales of 1 to 100 nm and simulation times up to microseconds. Differences in biomolecular binding can be analyzed as a function of crystallite size, facets, pH, concentration, temperature, and other solution conditions.^{40,42,43,45,67–73,75–77} Chemically consistent force fields for inorganic materials such as CHARMM-INTERFACE reproduce inorganic-aqueous and inorganic–organic interfacial properties with only 0% to 10% uncertainty relative to experiment.⁷⁴ For example, mechanisms of molecular recognition on silicates, aluminates, and metals have been identified using computation that are consistent with facet-specific trends, binding constants, and correlations with nanocrystal shape and yield observed in experiment.^{45,69,78,79}

Force field parameters and surface models for hydroxyapatite in similar accuracy have not yet been available.^{40,67} Earlier force fields coarsely represent chemical bonding and provide no validation of surface properties;^{80–86} in particular, realistic chemistry and pH in surface models have not been included. Associated problems include unjustified atomic charges, lack of validation of Lennard-Jones parameters, neglect of pH conditions, and incompatibility of the chosen energy expressions with common force fields for biomacromolecules and organic compounds. Arbitrary assignments of nonbond parameters have caused errors in excess of 100% in surface and interfacial properties. For example, the assumption of non-hydrated apatite surfaces at pH 15 in prior DFT and MD studies^{80–88} corresponds to conditions of immediate cell death, invalidating prior conclusions of specific binding of proteins and organic ligands (see details in section S1 in the Supporting Information).

These limitations are resolved by the present force field and surface models. (1) Atomic charges represent chemical bonding in balance with available experimental data on electron deformation densities, similar compounds across the periodic table, chemical reactivity, theoretical foundations in the Extended Born model, and quantum chemistry.^{74,89} (2) The chosen Lennard-Jones parameters are accompanied by a physical explanation in the context of similar compounds and validated against densities, surface energies, and hydration energies. (3) The surface models take into account common (001), (010), (020), and (101) facets of hydroxyapatite nanocrystals across a range of pH values (Figures 1 and 2).

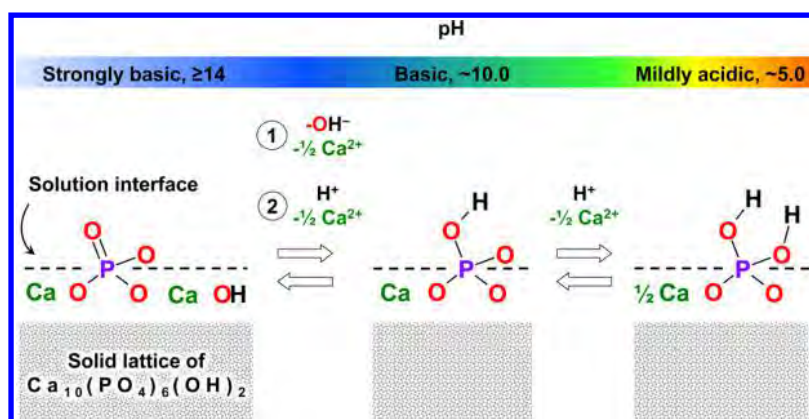


Figure 1. Schematic representation of HAP and the construction of surface models at different pH values. Interactions with water at pH values lower than 14 cause protonation and leaching of superficial hydroxide ions along with a stoichiometric amount of calcium ions. Increasing protonation of superficial phosphate ions leads to the formation of hydrogen phosphate and removal of a stoichiometric amount of calcium ions. At pH values lower than 10, further protonation of hydrogen phosphate to dihydrogen phosphate and removal of further calcium ions occurs. Surface models for a specific pH value can be customized by corresponding stoichiometric changes to pristine hydroxyapatite surfaces and associated redistribution of atomic charges to maintain overall charge neutrality. Changes in crystal phase can also be implemented, for example, to octacalcium phosphate at low pH values (see section 4 in the text).

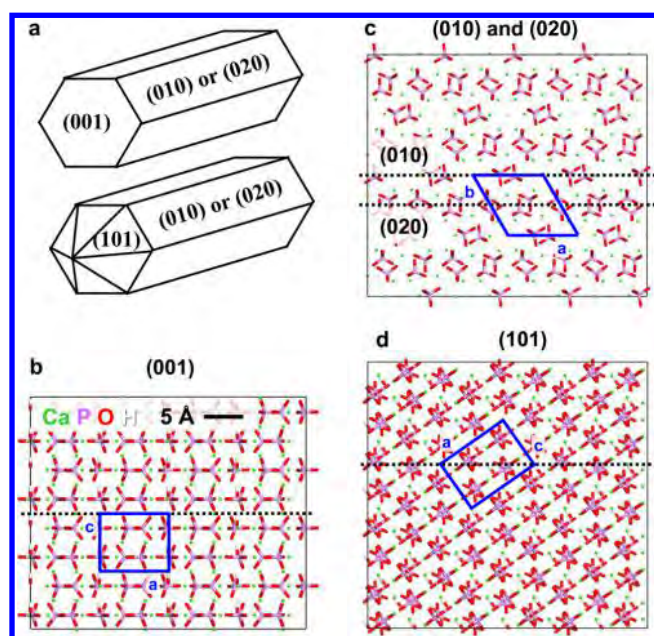


Figure 2. Nanocrystal shape and common cleavage planes of hydroxyapatite. (a) Schematic of the rod-like shape of HAP nanocrystals. (b) The basal plane (001). (c) The prismatic planes (010) and (020), respectively. (d) The (101) plane. Projections of the unit cell are shown in blue, and cleavage planes are shown as black dashed lines in side view. Models of cleaved surfaces are prepared by an equal 50/50 distribution of ions on both sides of the cleavage plane followed by thermal relaxation and energy minimization.

(4) The parameters are integrated into the INTERFACE force field and compatible with the force fields CHARMM, AMBER, GROMACS, PCFF, CVFF, and OPLS-AA, including standard water models such as SPC and TIP3P. Additional adjustable parameters to simulate the inorganic–organic interfaces are not needed. (5) Validation includes the density, IR spectrum, mechanical properties, surface properties, and interfacial properties with water including the range of pH values in which apatite is stable (3 to 15). Computed properties from molecular dynamics simulations are shown to be in excellent

agreement with experimental data, surpassing prior models up to 2 orders of magnitude in accuracy.

Therefore, the new force field and models will enable the quantitative analysis of an unlimited number of apatite surfaces and nanocrystals in combination with water, proteins, DNA, and organic molecules under realistic solution conditions in future work (see preview in refs 40 and 67). In the following sections, we introduce the parameters, the surface models, and explain facet-specific cleavage energies, hydration energies, as well as the structure of the HAP–water interfaces as a function of pH.

3. FORCE FIELD PARAMETERS

The force field parameters are described in this section. Full details of the derivation and the rationale for each parameters can be found in section S2 in the Supporting Information.

3.1. Choice of the Energy Expression. The hydroxyapatite parameters extend the INTERFACE force field⁷⁴ following a series of developments for clay minerals, silica, cement minerals, aluminates, metals, and calcium sulfates.^{43,68,72,90,91} The HAP parameters are compatible with the force fields PCFF, COMPASS, GROMACS, CVFF, DREIDING, CHARMM, AMBER, and OPLS-AA that cover solvents, organic molecules, and biopolymers. Broad compatibility supports the mission of the INTERFACE force field to unify materials oriented and biomolecular simulations into one single and accurate platform. The functional form of PCFF and COMPASS force fields consists of a quadratic potential for bond stretching and angle bending, a Coulomb potential, and a 9-6 Lennard-Jones potential, including Waldman-Hagler combination rules between different atom types i and j (eq 1):

$$\begin{aligned}
 E_{\text{total}} = & \sum_{\text{bonds}} K_{r,ij}(r_{ij} - r_{0,ij})^2 + \sum_{\text{angles}} K_{\theta,ijk}(\theta_{ijk} - \theta_{0,ijk})^2 \\
 & + \sum_{ij\text{nonbonded}} \frac{q_i q_j}{4\pi\epsilon_0 r_{ij}} \\
 & + \sum_{ij\text{nonbonded}} \epsilon_{ij} \left[2 \left(\frac{\sigma_{ij}}{r_{ij}} \right)^9 - 3 \left(\frac{\sigma_{ij}}{r_{ij}} \right)^6 \right]
 \end{aligned} \quad (1)$$

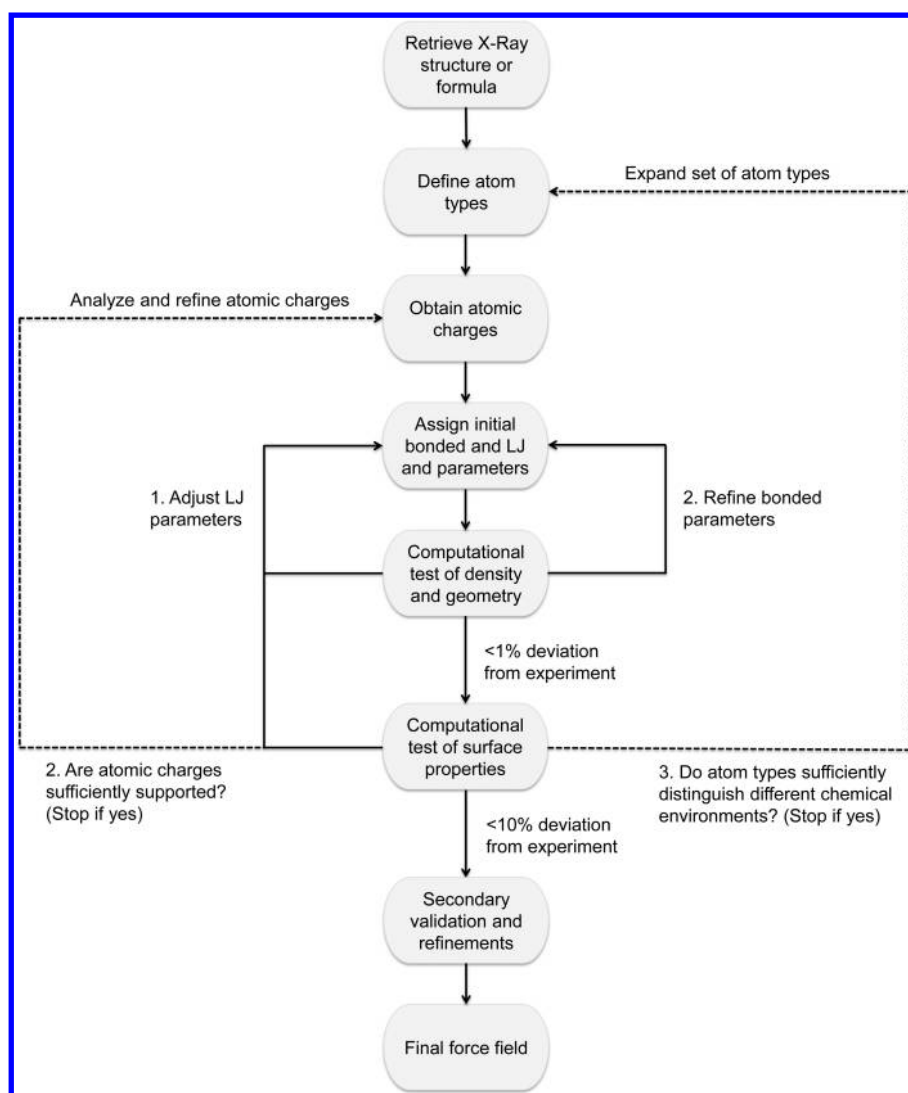


Figure 3. Flowchart for the parameter development for hydroxyapatite in the INTERFACE force field (from ref 74). The procedure is universal for compounds across the periodic table.

Table 1. Nonbonded Parameters for Bulk HAP and Protonated Surfaces^a

atom type	charge (e)	9-6 LJ parameters (PCFF, CFF, COMPASS)		12-6 LJ parameters (CHARMM, CVFF, AMBER, GROMACS, DREIDING, OPLS-AA)	
		σ_0 (Å)	ϵ_0 (kcal/mol)	σ_0 (Å)	ϵ_0 (kcal/mol)
Bulk Hydroxyapatite					
Ca	1.5	3.55	0.240	3.30	0.130
P	1.0	4.50	0.250	4.30	0.280
O in PO_4^{3-}	-0.8	3.50	0.055	3.40	0.070
O in OH^-	-1.1	3.80	0.080	3.70	0.080
H in OH^-	0.2	1.098	0.013	0.0001	0
Hydrated and Protonated Surface					
O in $(\text{HO})_n\text{PO}_{4-n}^{(3-n)-}$	-0.65			same as O in PO_4^{3-}	
O in $(\text{HO})_n\text{PO}_{4-n}^{(3-n)-}$	-0.6 to -0.8 ^b			same as O in PO_4^{3-}	
H in $\text{HPO}_4^{2-}/\text{H}_2\text{PO}_4^-$	0.4			same as H in OH^-	

^aThe parameters are listed for PCFF, CFF, COMPASS (9-6 Lennard-Jones potential), GROMACS, AMBER, CHARMM, DREIDING, CVFF, and OPLS-AA (12-6 Lennard-Jones potential). The 12-6 Lennard-Jones parameters are identical for AMBER and CHARMM due to the absence of 1,4 bonded atoms and identical combination rules for σ_0 (arithmetic) and ϵ_0 (geometric). CVFF and OPLS-AA use a geometric mean of σ_0 for different atoms that leads to practically identical results and requires no adjustments. ^bThe atomic charge on the oxygen atoms in protonated phosphates depends on the degree of protonation and on the (*hkl*) facet due to different stoichiometric amounts of dissolved calcium hydroxide. See discussion of surface models in section 4.

The force fields CVFF, CHARMM, GROMACS, DREIDING, AMBER, and OPLS-AA use a 12-6 Lennard-Jones potential instead of a 9-6 Lennard-Jones potential (eq 2):

$$E_{\text{total}} = \sum_{\text{bonds}} K_{r,ij}(r_{ij} - r_{0,ij})^2 + \sum_{\text{angles}} K_{\theta,ijk}(\theta_{ijk} - \theta_{0,ijk})^2 + \sum_{ij\text{nonbonded}} \frac{q_i q_j}{4\pi\epsilon_0 r_{ij}} + \sum_{ij\text{nonbonded}} \epsilon_{ij} \left[\left(\frac{\sigma_{ij}}{r_{ij}} \right)^{12} - 2 \left(\frac{\sigma_{ij}}{r_{ij}} \right)^6 \right] \quad (2)$$

The individual 12-6 force fields differ somewhat in combination rules for LJ parameters and in scaling factors for nonbond interactions between 1,4 bonded atoms. However, the differences are small enough to work with the same set of hydroxyapatite parameters (see further details of the energy expressions in section S2.1 in the Supporting Information).

3.2. Rationale for Parameter Derivation. The development of force field parameters follows the INTERFACE approach (Figure 3).⁷⁴ Key steps are (1) the definition of atom types, (2) the analysis of atomic charges, (3) the assignment of bonded terms and Lennard-Jones parameters, (4) successive validation and iteration of structural and energetic properties. Hydroxyapatite contains six distinct atom types, namely Ca²⁺ ions, P, O, and H atoms in phosphate and hydrogen phosphate, as well as O and H atoms in hydroxide ions. The analysis of chemical bonding by atomic charges shows that only Ca is predominantly ionic, all other atoms are predominantly covalent. Therefore, bonded terms are included for all nearest neighbor atoms except Ca, and nonbonded terms are included between all pairs of atoms (under observation of exclusions for 1,2 and 1,3 bonded atoms and scaling rules for 1,4 bonded atoms).

3.3. Atomic Charges. Atomic charges were assigned according to Heinz (Table 1).⁸⁹ Heinz charges intend to measure chemical bonding and electronic structure in a simple manner and achieve high accuracy when used in numerical computation (see details in section S2.3 in the Supporting Information). The atomic charge of calcium in hydroxyapatite was chosen as +1.5 ± 0.1e consistent with the minerals tricalcium silicate,⁴³ tricalcium aluminate,⁷² tobermorites, and gypsum that are chemically similar.⁷⁴ The atomic charge of the phosphorus atom in HAP was derived as +1.0 ± 0.1e from the X-ray deformation density of aluminum phosphate.⁹² The net atomic charge of the hydroxide ion in the mineral was set as -0.9 ± 0.1e, i.e., slightly below -1.0e, due to residual covalent bonding known in Ca(OH)₂.^{43,72,89,93} The atomic charges within the hydroxide ion are +0.2e for the hydrogen atom and -1.1e for the oxygen atom. To satisfy charge neutrality of hydroxyapatite, Ca₁₀(PO₄)₆(OH)₂, the atomic charge of the oxygen atom in the phosphate is -0.8e. This value is consistent with atomic charges for oxygen atoms in clay minerals and other oxides in a range of -0.5e to -0.9e, as well as with a known minimum of the electron affinity of oxygen near -0.6e to -0.7e.^{74,89} Upon protonation to hydrogen phosphates at lower pH, the difference between incoming proton charge and leaving calcium charge distributes over the oxygen atoms and decreases the oxygen partial charge in a range from -0.8e to -0.6e (see section 4 for details).

3.4. Bonded Parameters. Bonded parameters of HAP include equilibrium bond lengths $r_{0,ij}$, angles $\theta_{0,ijk}$, harmonic bond stretching coefficients $K_{r,ij}$, and harmonic angle bending coefficients $K_{\theta,ijk}$ (eqs 1 and 2). The parameters were derived from experimental X-ray data and vibration spectra, including small adjustments to reproduce experimental bond lengths with <1% deviation in NPT molecular dynamics simulation at 298 K (Table 2). $r_{0,ij}$ amounts to 1.57 Å for P–O bonds, to 0.94 Å for

Table 2. Bonded Parameters for Bulk HAP and Protonated Surfaces^a

bond type	$r_{0,ij}$ (Å)	$K_{r,ij}$ [kcal/(mol Å ²)]
P–O bonds in PO ₄ ³⁻ , HPO ₄ ²⁻ , H ₂ PO ₄ ⁻	1.570	430
O–H bonds in HPO ₄ ²⁻ , H ₂ PO ₄ ⁻ and OH ⁻	0.940	500
angle type	$\theta_{0,ijk}$ (deg)	$K_{\theta,ijk}$ [kcal/(mol rad ²)]
O–P–O in PO ₄ ³⁻ , HPO ₄ ²⁻ , H ₂ PO ₄ ⁻	109.47	125
P–O–H in HPO ₄ ²⁻ , H ₂ PO ₄ ⁻	115.0	50
dihedral type	$\varphi_{0,ijkl}$ (deg)	$K_{\varphi,ijkl}$ (kcal/mol)
H–O–P–O in HPO ₄ ²⁻ , H ₂ PO ₄ ⁻	0	0

^aThe bonded parameters are identical for all energy expressions (eqs 1 and 2).

O–H bonds in protonated phosphate and in hydroxide ions. The equilibrium angle $\theta_{0,ijk}$ of O–P–O bending is 109.47° consistent with XRD studies and sp³ hybridization (Table 2).^{94–96} The angle for H–O–P bonds in protonated phosphate ions was assigned as 115° in analogy to parameters for clay minerals.⁹⁰ Average computed bond angles in NPT molecular dynamics simulation deviate less than 1% from XRD data under standard conditions.

The harmonic force constants for bond stretching $K_{r,ij}$ and angle bending $K_{\theta,ijk}$ were tuned to reproduce the experimental IR spectrum and agree within ±50 cm⁻¹ (Figure 4). Three

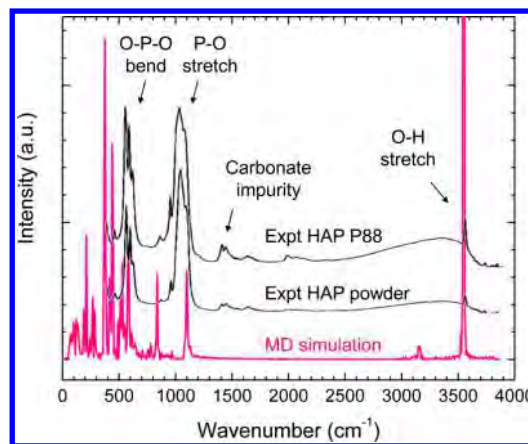


Figure 4. IR spectrum of hydroxyapatite in experiment and in molecular dynamics simulation (MD). Experimental FTIR spectra were recorded for HAP P88 (Plasma Biotol) and HAP powder (Merck), see ref 99. The computed spectrum equals a superposition of IR and Raman signals.

major IR bands of hydroxyapatite are observed, including O–H stretching at 3600 cm⁻¹, P–O stretching at 1100 cm⁻¹, and O–P–O bending at 600 cm⁻¹.^{97–100} The IR band at 3600 cm⁻¹ originates from the bond stretching coefficient of O–H bonds in hydroxide ions and in hydrogen phosphate ($K_{r,ij} = 500$ kcal/(mol Å²)). The P–O stretching band at 1100 cm⁻¹ is represented by the P–O stretching constant $K_{r,ij} = 430$ kcal/

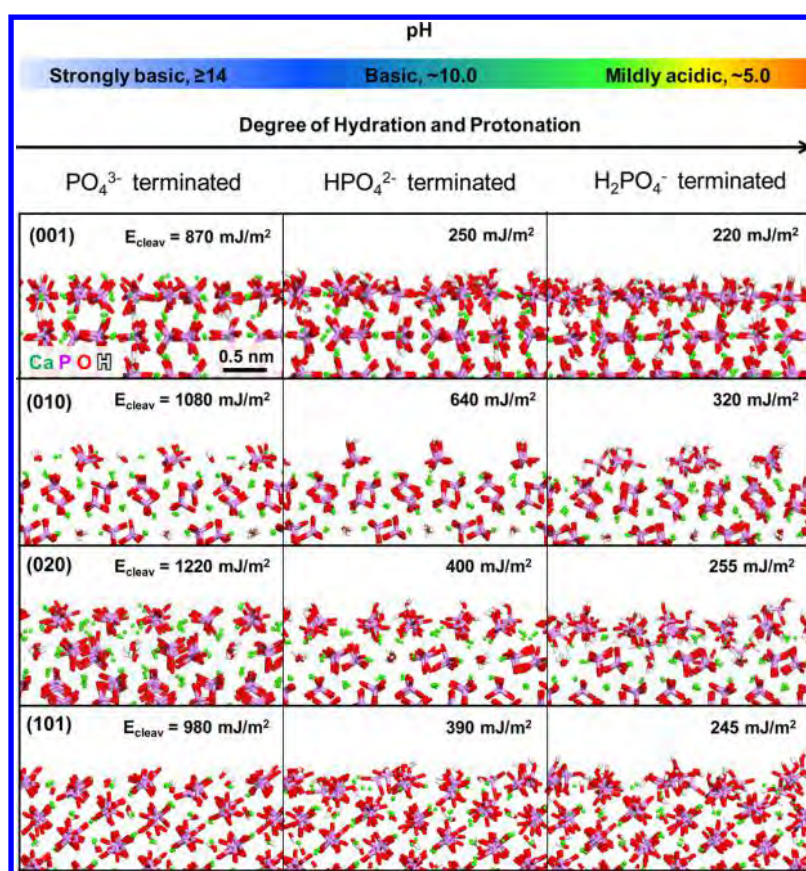


Figure 5. Side view of equilibrium model surfaces of hydroxyapatite and computed cleavage energies in vacuum at different pH values. (001), (010), (020), and (101) surfaces. The left column shows the surfaces before hydration (pH >14), the middle column shows the surfaces with monohydrogen phosphate termination (pH ~ 10), and the right column visualizes the surfaces with dihydrogen phosphate termination (pH ~ 5). For all facets, increasing surface hydration and protonation increase surface reconstruction, surface disorder, and decrease the cleavage energy. This trend correlates with decreased charge density per unit area as the pH value decreases from 14 to 5. The cleavage energies also show notable facet-specific detail. Protonation was limited to the topmost molecular layer in the models. The stated cleavage energies are average values from 9-6 and 12-6 potentials and have an uncertainty of ± 10 to $\pm 20 \text{ mJ/m}^2$ (see Table 6).

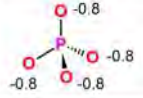

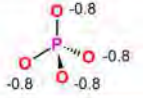
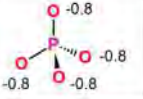
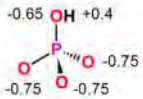
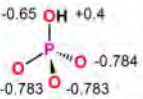

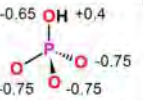
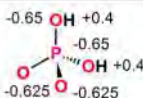
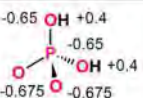
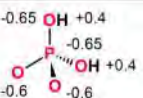
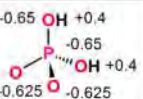
($\text{mol } \text{\AA}^2$). The angular O–P–O vibrations of isolated phosphate groups in hydroxyapatite at 600 cm^{-1} are described with $K_{\theta,ijk} = 125 \text{ kcal}/(\text{mol rad}^2)$ (Figure 4). Further details can be found in section S2.4 in the Supporting Information.

3.5. Lennard-Jones Parameters. Lennard-Jones parameters are essential to reproduce the density and surface properties (Table 1).^{68,74,90} The nonbond diameter σ_0 represents the van der Waals size of each atom type and is approximately known for all elements and ions across the periodic table.^{62,101} The actual values of σ_0 in the force field commonly fall within a $\pm 10\%$ range of the tabulated van der Waals sizes depending on the chemical environment; larger values σ_0 often serve to compensate attractive electrostatic interactions in significantly ionic systems. The primary function of σ_0 is the reproduction of the experimentally observed density. The parameter ϵ_0 correlates in first order approximation with the polarizability of each atom type. In highly charged systems, significantly increased values ϵ_0 also help counteract strong electrostatic attraction. The validation of ϵ_0 ultimately requires the reproduction of a cleavage energy, hydration energy, or other surface property at 298 K, which typically leads to reliable predictions of several associated properties as well (e.g., thermal, mechanical).^{43,74,90} Such validation plays a critical role since it calibrates the classical Hamiltonian to reproduce correct energies in addition to the reproduction of correct structures.

LJ parameters for the atom types in hydroxyapatite, as also the other parameters, are similar to those in silicates and gypsum as a consequence of similar chemical bonding and coordination environments (Table 1).^{43,68,74} The van der Waals diameter σ_0 of calcium is 3.55 \AA in the 9-6 LJ potential and 3.30 \AA in the 12-6 potential, slightly larger than for a fully ionized Ca^{2+} ion due to some covalent character in the minerals.^{62,101} Phosphorus is represented by a σ_0 value of 4.50 \AA in the 9-6 LJ potential and 4.30 \AA in the 12-6 LJ potential, similar to silicon in silicates. σ_0 values of oxygen atoms in phosphate are 3.50 and 3.40 \AA in the 9-6 and 12-6 LJ potential, respectively, similar to oxygen in silicates. σ_0 values of oxygen atoms in hydroxide are somewhat larger at 3.80 and 3.70 \AA , respectively, due to a higher negative charge and required repulsion (Table 1).

The nonbonded well depth ϵ_0 of calcium was set to 0.24 kcal/mol in PCFF and equivalently to 0.13 kcal/mol in CHARMM (Table 1). This comparatively large nonbonded well depth, especially in the 9-6 Lennard-Jones potential, strengthens the repulsive part of the potential to counterbalance strong Coulomb attraction. The value ϵ_0 for phosphorus is 0.25 and 0.28 kcal/mol , respectively. Nonbond well depths were chosen as 0.055 and 0.07 kcal/mol for oxygen atoms in phosphates, respectively, and a somewhat higher value ϵ_0 of 0.08 kcal/mol was assigned to hydroxide related to the higher charge (Table 1).

Table 3. Details of Hydroxyapatite Surface Models^a

Property	Facet and surface area (Å ²)			
	(001)	(010)	(020)	(101)
	32.6214×37.6680	37.6678×34.3750	37.6678×34.3750	34.9787×32.6214
pH >14, PO₄³⁻ terminated, cleavage as-is				
atomic charges on phosphate ions ^b				
pH ~10, HPO₄²⁻ terminated				
# of hydroxide ions removed ^c	16	20	0	12
# of phosphate ions protonated ^c	48	20	40	36
# of calcium ions removed ^c	32	20	20	24
atomic charges on surface phosphate ^b				
pH ~5, H₂PO₄⁻ terminated				
# of hydroxide ions removed ^c	16	20	0	12
# of phosphate ions protonated ^c	48	20	40	36
# of calcium ions removed ^c	56	30	40	42
atomic charges on surface phosphate ^b				

^aAtomic charges and stoichiometric changes are indicated as a function of protonation state and facet for a chosen surface area (~12 nm²), assuming hydration and protonation in the topmost molecular layer. ^bThe charge on the phosphorus atom was +1.0 *e* for all pH values. ^cAt the topmost surface layer. The number of hydroxide ions removed and the number of phosphate ions protonated corresponds to the total number of ions available. In case of the (010) facet, the surface is corrugated and only 20 phosphate ions in the upper half of the topmost layer were considered and modified. Together with the somewhat less accessible lower half, 40 phosphate ions could alternatively be chosen to belong to the top layer.

For the transcription of parameters from the 9-6 LJ potential to the 12-6 LJ potential, van der Waals diameters σ_0 were reduced by approximately 5%. The well depth ϵ_0 in the 12-6 form tends to be larger than in the 9-6 form in case it represents dispersive interactions; the higher value then compensates the stronger repulsion at shorter distance in the 12-6 Lennard-Jones potential.⁹⁰ However, the well depth ϵ_0 in the 12-6 form can be smaller in case it represents repulsion (e.g., for Ca²⁺); this is then owed to the more repulsive nature of the 12-6 LJ potential compared to the 9-6 LJ potential. The final set of parameters was obtained upon thorough validation of density, cell geometry, as well as cleavage energy in over 500 individual tests (see details in section S2.5 in the [Supporting Information](#)).

4. SURFACE MODELS OF HYDROXYAPATITE AS A FUNCTION OF PH

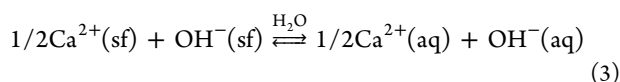
A critical aspect for modeling of apatite surfaces is the strong pH dependence of the surface chemistry. Realistic models make the difference between quantitative predictions and no predictions at all, similar to silica surfaces.^{41,42,68} A number of independent experimental studies explain changes in surface composition upon cleavage and hydration and are a great starting point to inform appropriate models.^{46–62} The surface

chemistry correlates strongly with the distinct pK values of phosphoric acid of 2.15 (pK₁), 7.20 (pK₂), 12.32 (pK₃), as well as the pK value of water of 15.7 (pK_w) at 298 K.⁶² The implementation in apatite models is an indispensable requirement for meaningful simulations of aqueous and biomolecular apatite interfaces.⁴⁰ Cleavage, hydration, and protonation of the surfaces lead to realistic atomistic surface models and are described in the following.

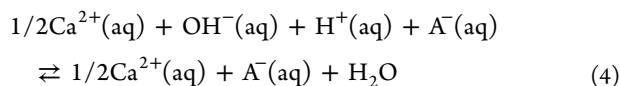
4.1. Cleavage. The number of possible (*h k l*) cleavage planes is in principle unlimited while cleavage preferably occurs in (*hkl*) directions with weaker nonbonded interactions. Common cleavage planes of hydroxyapatite are known from experiment and include the (001), (010), (020), and (101) surfaces (Figure 2). Surface models were created accordingly by equally dividing charged ions between the two newly created surfaces upon cleavage, followed by relaxation in molecular dynamics simulation to minimize local electric fields (Figure 5).^{43,72,102,103} Surface reconstruction leads to two low energy surfaces that are both charge-neutral (see details in section S3.1 in the [Supporting Information](#)). The cleavage energy in vacuum is a measure of cohesion in the mineral at 298 K and suitable to validate the force field against experimental data.

4.2. Hydration and Influence of pH. Freshly cleaved surfaces of hydroxyapatite are hygroscopic and immediately

attract water (or carbon dioxide) in air. Calcium and hydroxide ions form a superficial hydrated layer of calcium hydroxide:

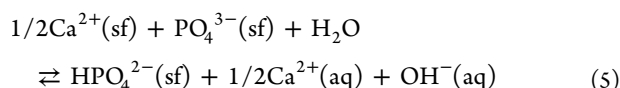


$\text{Ca}^{2+}(\text{sf})$ and $\text{OH}^{-}(\text{sf})$ hereby denotes the ions at the top atomic layer of the surface and $\text{Ca}^{2+}(\text{aq})$ and $\text{OH}^{-}(\text{aq})$ the corresponding hydrated species in contact with water. The hydrated surfaces are only stable in solution at pH values above ~ 14 as the $\text{p}K_{\text{a}}$ value of water is 15.7.⁶² Lower pH values cause neutralization of the superficial hydroxide ions and leaching of the hydroxyapatite surface driven by acids (H^+A^-) in a buffered solution:



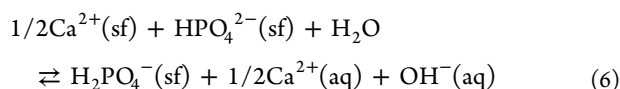
Since pH values above pH 14 are practically uncommon in living organisms, the apatite surface is hardly ever present in chemically pure form. Hydration and protonation reactions cause leaching of calcium hydroxide in the form of other calcium salts. The concentration of OH^{-} ions at the immediate surface of hydroxyapatite is very high (on the order of 1 mol/L), and due to the ion product of water $K_{\text{w}} = [\text{H}^+][\text{OH}^-] = 10^{-14} \text{ M}^2$ any buffer system with a pH value less than 14 neutralizes superficial hydroxide ions (Figure 1).

The next process at pH values below 13 is the protonation of superficial phosphate ions to monohydrogen phosphate ions (HPO_4^{2-}):



This reaction is related to the $\text{p}K_3$ value of 12.3 of phosphoric acid and causes further leaching of calcium hydroxide in subsurface layers. At a pH value of ~ 12.0 , the surface layer consists approximately of a 50/50 mixture of phosphate and hydrogen phosphate ions. The net reactions and changes in surface chemistry at high pH are summarized in Figure 1.

A maximum amount of monohydrogen phosphate ions on the top surface layer near 100% is then expected at pH ~ 10.0 , close to the average of $\text{p}K_2$ and $\text{p}K_3$ of 9.75. A further decrease in pH value causes the protonation of monohydrogen phosphate to dihydrogen phosphate ions (H_2PO_4^-):



The associated $\text{p}K_2$ value of H_3PO_4 is 7.2 and leads to a 50/50 equilibrium mixture of hydrogen phosphate and dihydrogen phosphate ions on the surface at pH ~ 7.5 . This observation is consistent with the observed ratio of 31:69 at pH ~ 7.0 by IR spectroscopy in experiment.⁶¹ Finally, full coverage of the top surface layer with H_2PO_4^- ions is expected at a pH value of ~ 5.0 near the average of $\text{p}K_1$ and $\text{p}K_2$ of 4.7.

Below pH 5, surface termination may involve dihydrogen phosphate as well as phosphoric acid. Decreasing pH values also cause deeper penetration of water and protonation of phosphate ions up to many atomic layers beneath the surface atomic layer so that the chemical composition differs from "hydroxyapatite". The dissolution of hydroxide ions can lead to the precipitation of layered octacalcium phosphate; this process

may begin already below pH 8.^{59,60} The ionization state of the surfaces also depends somewhat on the total ionic strength in solution and on the type of present ions.^{41,47,104–106} In atomistic models, a distinction with a resolution of about 0.5 pH units appears to be sufficient for most purposes, especially in consideration of previous studies that assumed unrealistic pH values of 14 to examine processes under physiological conditions.^{80–88}

4.3. Implementation in Models. Model building of the apatite (*hkl*) surfaces and nanocrystals terminated by such facets for the different pH values involves cleavage, adjustments in the stoichiometry, and in atomic charges (Table 3). Stoichiometric adjustments are applied to the ions in the surface layer and in the desired number of subsurface layers; here only the surface layer was considered. The procedure is as follows: (1) cleave the (*hkl*) plane and relax the surface by annealing and energy minimization, (2) implement changes in stoichiometry according to the desired degree of hydration and protonation (Figure 1), (3) adjust atomic charges according to the formation of new bonds and departure of ions from the surface (for example, adjustments from P–O bonds to P–O–H bonds when hydrogen atoms from water bind to phosphate ions and calcium and hydroxide ions depart), (4) arrange cations and anions on the surface such that local electric fields and the overall energy are minimal using annealing and molecular dynamics. In the process, overall charge neutrality of the surfaces must be maintained⁸⁹ and associated charge increments/decrements must reasonably describe changes in chemical bonding and in the true electron density distribution.^{68,72}

The procedure is simple, effective, and easy to customize. Upon further changes in pH, only the charges of the oxygen atoms in phosphate ions require modification while all other bonded and nonbonded force field parameters can be kept the same (Table 3). The protocol can be applied to prepare models of any (*hkl*) apatite surface and apatite nanocrystals. Customization for different degrees of water penetration and substitution of cations and anions, such as Mg^{2+} , F^- , Cl^- , HCO_3^- , and CO_3^{2-} is also straightforward.

4.4. Comparison with Experimental Data. The proposed models correlate well with laboratory measurements of acid–base equilibria, solubility products, adsorption isotherms, AFM, SEM, TEM, IR and NMR spectroscopy, XPS, and Auger electron spectroscopy (see details in section S3.2 in the Supporting Information).^{45–61} The implementation in molecular models could perhaps be the most significant contribution in this work since experimental data have been available for decades and not been used. The surface reactions described in eqs 3 to 6 agree quantitatively with measurements and closely follow the protonation equilibria of water and phosphoric acid. IR spectroscopy has shown that the apatite surface consists of HPO_4^{2-} and H_2PO_4^- ions in a ratio of 31:69 at pH 7 in water,⁶¹ in agreement with an expected 50:50 ratio at pH 7.20 that equals the $\text{p}K_2$ value for H_2PO_4^- ions. Previous studies have also shown that the degree of ionization on crystal surfaces with pH sensitive groups tends to be slightly lower in comparison to the same process in solution due to dense packing and increased ion–ion repulsion per unit area on the crystal surface.⁶⁸ Therefore, a 50:50 equilibrium between HPO_4^{2-} and H_2PO_4^- ions on the apatite surface may be expected at pH ~ 7.5 rather than at pH = $\text{p}K_2 = 7.2$.

Solubility measurements and NMR data have shown that the Ca:P ratio of 1.67 in native apatite ($\text{Ca}_{10}(\text{PO}_4)_6(\text{OH})_2$)

Table 4. Lattice Parameters of Hydroxyapatite in Experiment and in NPT Molecular Dynamics Simulation with the INTERFACE-PCFF and INTERFACE-CHARMM Force Field at 298.15 K and 101.3 kPa

method	cell dim.	<i>a</i> (Å)	<i>b</i> (Å)	<i>c</i> (Å)	α (deg)	β (deg)	γ (deg)	density (g/cm ³)
expt ^a	2 × 2 × 1	18.83	18.83	13.75	90	90	120	3.160
force field 9-6	2 × 2 × 1	18.82	18.81	13.75	90.00	90.00	120.02	3.167
force field 12-6	2 × 2 × 1	18.78	18.77	13.95	90.00	90.00	119.99	3.135

^aReference 95.**Table 5.** Elastic Moduli and Elastic Constants in Experiment and in Simulation with the INTERFACE Force Field in 12-6 and 9-6 form (in GPa)^a

method	moduli			elastic constants				
	<i>K</i>	<i>E</i> _{iso} ^h	<i>G</i> _{iso} ^h	<i>C</i> ₁₁	<i>C</i> ₃₃	<i>C</i> ₄₄	<i>C</i> ₁₂	<i>C</i> ₁₃
expt ^b	89.0	114	44.5	137	172	39.6	42.5	54.9
force field 9-6 ^c	72.9	112	45.7	130	157	44.8	35.6	45.8
force field 12-6 ^c	81.3	121	48.5	147	185	47.5	47.3	43.1
FF-Buckingham ^d	90	118.8	46.6	134.4	184.7	51.4	48.9	68.5
DFT/PAW-PBE ^e	84.5	120.6	47.7	140.0	174.8	47.5	42.4	58.3
DFT/PBE ^f	90.7	106.6	46.6	145.2	191.4	37.6	47.8	73.6
DFT/GGA ^g	82	132.1	51.7	117.1	231.8	56.4	26.2	55.6

^aThe bulk modulus *K*, the isotropic Young's modulus *E*_{iso}, and the isotropic shear modulus *G*_{iso} are shown. Data from earlier simulations and density functional methods are also shown. ^bIsotropic elastic moduli were measured on polycrystalline specimens of hydroxyapatite and single crystal fluoroapatite with an uncertainty of ±1% (*K*, *E*_{iso}, *G*_{iso}). Elastic constants for hydroxyapatite were then calculated using theory. See refs 110–112. ^cThe uncertainty in computed elastic constants is ±1%. ^dReference 113. ^eReference 107 using DFT/PAW-PBE. ^fReference 108. ^gReference 109. ^hUsing VRH approximation, ref 114.

decreases on the surfaces to about 1.5 as a consequence of the altered stoichiometry upon hydration (Figure 1).^{47,50,54} At lower pH, the Ca:P ratio was reported to decrease below 1.0, which is consistent with the presence of HPO₄²⁻ and H₂PO₄⁻ ions (CaHPO₄ and Ca(H₂PO₄)₂, respectively).^{59,60} The exact Ca:P balance is dependent on pH as well as crystal facet and accordingly represented in the proposed models (Table 3). It further depends on how many molecular layers on the surface are considered in the measurement or calculation as the composition approaches bulk hydroxyapatite in the interior.

The depth of the hydrated and protonated layer was estimated to be about 1 nm in experiment⁵⁰ and could extend up to several nanometers at lower pH.^{59,60} The proposed surface models currently assume changes only in the first layer of phosphate ions for simplicity (~0.5 nm). The surface models are contained in the latest release of the INTERFACE force field (v1.5) and attached in the Supporting Information as a separate file including documentation. Extensions to any number of modified subsurface layers can be made as described in section 4.3 (Table 3 and Figure 5).

5. VALIDATION OF STRUCTURAL, VIBRATIONAL, AND MECHANICAL PROPERTIES

5.1. Structural Properties. Computed bond lengths, angles, and nonbonded interatomic distances in NPT simulations of bulk hydroxyapatite agree quantitatively with XRD measurements at room temperature.⁹⁵ Average bond lengths of P–O and O–H bonds are 1.54 ± 0.01 and 0.95 ± 0.01 Å, respectively, and O–P–O bond angles are 109.5° ± 0.2°. The deviation from experiment is less than 1%. Nonbonded interatomic distances between calcium ions and oxygen atoms in phosphate and hydroxide ions are between 2.4 and 2.6 Å in the simulation and depart less than 2% from X-ray data. Computed lattice parameters in NPT simulation agree with measurements on average within ±0.5% (Table 4). Deviations slightly over 1% occur for the cell parameter *c* using

the 12-6 Lennard-Jones potential, related to stronger repulsive interactions. (Further customization of parameters to reduce the deviation appear not necessary.) The excellent reproduction of bonded and nonbonded interatomic distances, angles, and lattice constants is a testimony to chemically meaningful atomic charges, bonded parameters, and van der Waals (LJ) parameters.

5.2. Vibrational Properties. The simulated vibration spectrum represents a superposition of infrared and Raman signals and shows a good match in wavenumbers with experimental data (Figure 4). The bands agree within 50 cm⁻¹ and include O–H stretching of hydroxide ions and OH groups at 3600 cm⁻¹, P–O stretching of phosphate at 1100 (strong) and 900 cm⁻¹ (weak), as well as O–P–O bending at ~600 cm⁻¹. Relative intensities and lattice modes below 400 cm⁻¹ are difficult to reproduce due to the lack of the full electronic structure in the force field. The experimental spectra also show broad signals for impurities such as water (from 3200 to 3500 cm⁻¹) and carbonates (near 1500 cm⁻¹) that do not appear in the simulation for pure hydroxyapatite.⁹⁹ The correlation between computed and experimental IR frequencies reflects the quality as well as limitations of the force field parameters.

5.3. Mechanical Properties. Computed mechanical properties deviate up to 20% relative to experiment, similar to values reported by earlier DFT calculations^{107–109} (Table 5). Hydroxyapatite possesses five independent elastic constants due to hexagonal symmetry. Isotropic Young's moduli *E*_{iso}, bulk moduli *K*, and isotropic shear moduli *G*_{iso} of polycrystalline HAP samples were previously measured using ultrasonic interferometry and then converted into elastic constants using data on closely related fluoroapatite single crystals (Table 5).^{110–112} The 12-6 LJ potential yields slightly higher moduli and diagonal elastic constants in comparison to the 9-6 LJ potential. For example, *C*₁₁ and *C*₃₃ are 10% higher than experimental data using the 12-6 potential and 10% lower using

the 9-6 potential. Somewhat higher stiffness using the 12-6 LJ potential results from the stronger repulsive part of the potential while atomic charges and bonded parameters are assumed to be the same for chemical consistency and simplicity. The anisotropic mechanical properties of HAP are well reproduced by 12-6 and 9-6 force fields as seen from the elastic constants C_{11} and C_{33} .

The computed values C_{44} , C_{12} , and C_{13} from PBE and GGA density functionals are notably less accurate in comparison to the force field, which performs very well considering the simplicity and a million times lower computational cost compared to DFT. A larger set of previous force field parameters using a Buckingham potential that was specifically parametrized to match elastic constants by de Leeuw et al. shows better match in elastic moduli but higher deviations of C_{44} , C_{12} , and C_{13} compared to the force field reported here as well.¹¹³ Therefore, the INTERFACE force field achieves very good agreement in elastic constants with experiment, in part even better than sophisticated quantum mechanical calculations.^{107–109}

6. CLEAVAGE ENERGY OF NEAT AND PROTONATED HYDROXYAPATITE SURFACES IN VACUUM

6.1. Cleavage Energy of Neat Hydroxyapatite Surfaces. Similar to other minerals such as calcium silicates and clay minerals, surfaces of HAP reconstruct upon cleavage and do not recover the perfect original crystal structure upon agglomeration.^{43,102} Solid–vapor interface tensions are therefore not uniquely defined. A suitable measure for the surface energy of (*hkl*) planes is therefore the cleavage energy (Figure 5 and Table 6).¹⁰³ Molecular dynamics simulation was employed to monitor the cleavage of the common low index planes (001), (010), (020), and (101) of HAP in vacuum (Figure 5). (*0n0*) planes are thereby equivalent to (*n00*) planes as a result of the hexagonal crystal symmetry. The computed cleavage energies upon slow, electroneutral cleavage of the neat phosphate-terminated surfaces range from 870 to 1220 mJ/m². The cleavage energy increases in the order (001) < (101) < (010) < (020) and consists of over 90% Coulomb energy and less than 10% van der Waals energy for all planes.¹⁰²

In experiment, the freshly cleaved surfaces are challenging to study as they are hygroscopic, and thus sensitive to air and moisture (see section 4).^{46–62} Direct measurements of cleavage energies in vacuum were thus not reported to our knowledge. Nevertheless, cleavage energies of minerals of comparable chemical composition were previously measured and computed cleavage energies for hydroxyapatite are in good relative agreement (Table 6).^{43,74} Cleavage energies of calcium oxide and calcium hydroxide, for example, were measured by Brunauer to be 1300 and 1180 mJ/m² (± 100 mJ/m²).⁹³ Facet-averaged cleavage energies for HAP are expected slightly lower since the phosphate ions in $\text{Ca}_{10}(\text{PO}_4)_6(\text{OH})_2$ are less polar than oxide or hydroxide ions (section 3).⁸⁹ The facet-averaged cleavage energy of HAP is dominated by the prismatic (010) and the basal (001) planes (Figure 2) and computed as 1000 ± 50 mJ/m², in agreement with expectations of a cleavage energy slightly lower than that for calcium oxide and calcium hydroxide (Table 6). In contrast, computed cleavage energies using prior Buckingham potentials¹¹⁵ and DFT calculations²⁷ are clearly overestimated at 1300 and 1700 mJ/m² (see further comparisons in section S3.3 in the Supporting Information).

The calculations further show that the cleavage energy of hydroxyapatite notably depends on crystal facet (Figure 5 and

Table 6. Computed Cleavage Energy of Hydroxyapatite Facets in Neat and Hydrated Form in Comparison to Available Experimental Data in Vacuum^a

Method	Cleavage energy			
	Basal plane (001)	Prismatic plane (010)	(020)	(101)
1. HAP surface as-is (PO_4^{3-} terminated)				
Force field 9–6	880	1076	1234	984
Force field 12–6	869	1092	1213	973
Buckingham potential ^b	~ 1100	~ 1310	~ 1048	
DFT-B3LYP ^c	1058	1709	NA	1646
<i>Related experimental data</i>				
HAP	NA			
CaO (more ionic) ^d	1310 \pm 200 (facet average)			
Ca(OH) ₂ (more ionic) ^d	1180 \pm 100 (facet average)			
2. HAP surfaces, HPO_4^{2-} terminated (pH ~ 10)				
Force field 9–6	250	658	411	369
Force field 12–6	243	618	386	408
3. HAP surfaces, H_2PO_4^- terminated (pH ~ 5)				
Force Field 9–6	225	330	250	271
Force Field 12–6	222	312	262	221
<i>Related experimental data (similar compounds near pH 7)</i>				
Fluoroapatite ^e	95 \pm 25	480 \pm 30 ((010) and (020))		NA
$\text{CaSO}_4 \cdot 2 \text{H}_2\text{O}^f$	352 \pm 20 (facet average)			
$\text{Ca}_3\text{Si}_2\text{O}_7 \cdot 7 \text{H}_2\text{O}^g$	386 \pm 20 (facet average)			

^aData are given in mJ/m². The uncertainty of computed values is ± 25 mJ/m², supported by the difference between 12-6 and 9-6 force fields.

^bBuckingham potential, ref 115. ^cQuantum mechanical calculations, ref 27.

^dReference 93. ^eReference 116. Slow cleavage of fluoroapatite (FAP) was performed at the basal and prismatic planes. Simultaneous hydration is likely to play a role and the data are therefore somewhat uncertain. The cleavage energy for the prismatic plane may include contributions by (010) and (020) facets. ^fGypsum, ref 119.

^gTobermorite, ref 118.

Table 6). The (001) surface of HAP is of lowest cleavage energy with ~ 870 mJ/m² according to simulation. Cleavage of the (001) surface involves redistribution of calcium ions on the nascent surfaces, minor surface reconstruction, and comparatively minor local electric fields arise at the cleavage sites. Cleavage of the (101), (010), and (020) planes comprises the distribution of larger phosphate ions. The (101) surface is then of approximately 10% higher cleavage energy with ~ 980 mJ/m² according to the simulation, and reorientation of phosphate ions can be seen (Figure 5). The (010) and (020) surfaces exhibit the highest cleavage energy of ~ 1080 and ~ 1220 mJ/m² as phosphate ions with multiple negative charges are separated upon cleavage, accompanied by significant surface reconstruction and generation of noticeable local electric fields. For example, calcium ions on the (020) surface beneath the superficial layer of phosphate ions move to the outer surface upon cleavage to better shield the concentration of negative charge at the cleavage plane (Figure 5).

6.2. Remaining Cleavage Energy of Protonated Hydroxyapatite Surfaces. The surface energy of the protonated hydrogen phosphate and dihydrogen phosphate terminated surfaces at lower pH can be quantified by remaining cleavage energies in vacuum (Figure 5 and Table 6).^{46–50} These energies are determined in a two-step process that involves (1) agglomeration of two equilibrated protonated

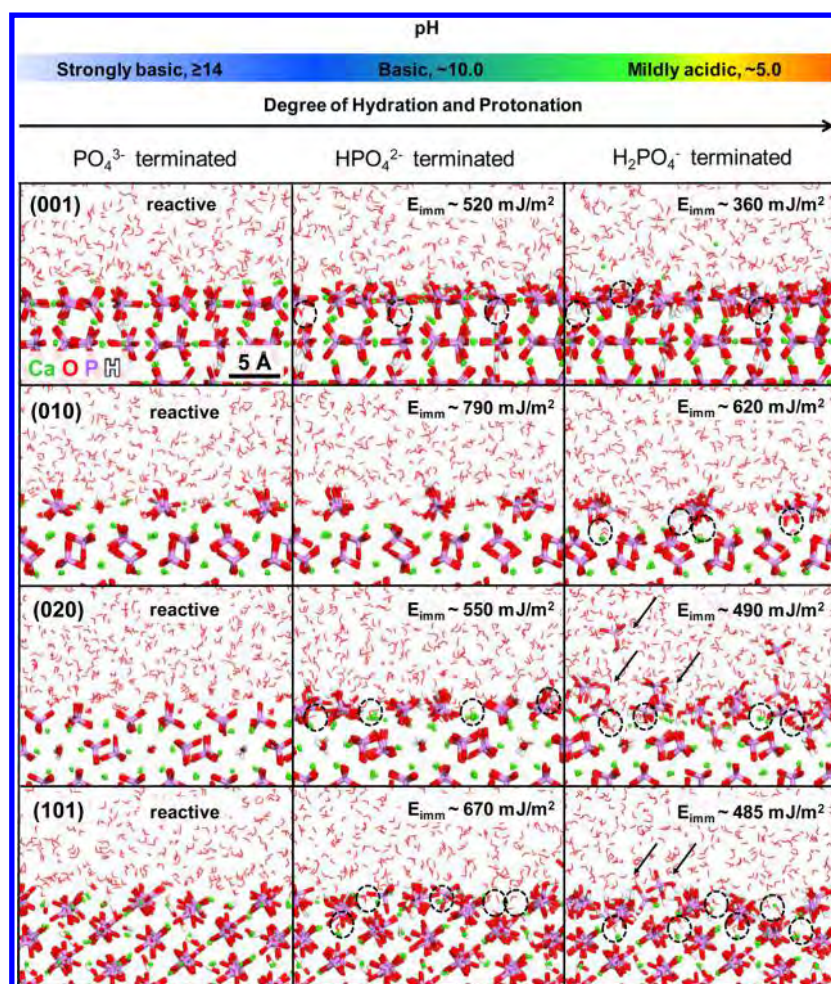


Figure 6. Snapshots of hydroxyapatite–water interfaces at different pH and computed energy of immersion (= energy of hydration without negative sign). Freshly cleaved, PO_4^{3-} terminated surfaces are reactive and only stable at very high pH (left column). Surfaces terminated by HPO_4^{2-} ions at $\text{pH} \sim 10$ exhibit significant, facet-specific immersion energies (middle column). Dashed black circles highlight penetration of water molecules into the surface of the crystal lattice. Surfaces terminated by H_2PO_4^- ions at $\text{pH} \sim 5$ exhibit lower immersion energies (right column). Protonated phosphate ions on the surface are more mobile, assume random orientations, and partially dissolve from the surface, especially from (020) and (101) surfaces, as observed also in experiment (indicated by black arrows). The stated immersion energies are average values from 9-6 and 12-6 potentials and have an uncertainty of ± 10 to ± 30 mJ/m^2 (see Table 7).

surfaces followed by (2) renewed cleavage and relaxation of the separated surface in molecular dynamics simulation. Perfect cleavage is then no longer possible and an uncertainty of $\pm 5\%$ is expected due to the overall series of modifications including original cleavage of the neat surfaces, protonation, agglomeration, and renewed separation of the agglomerated surfaces using molecular dynamics simulation to compute the remaining cleavage energies.⁴³

The partial loss of calcium ions and the presence of less negatively charged protonated phosphate ions on the surfaces $\text{pH} \sim 10$ (Figure 1) reduce the remaining cleavage energy by 40% to 70% relative to the original cleavage energy of the bulk mineral, and two protonation steps at $\text{pH} \sim 5$ reduce the remaining cleavage energy by 70% to 80% relative to the original cleavage energy. The remaining cleavage energies also indicate that individual (*hkl*) cleavage planes respond differently to hydration and protonation. The data furthermore suggest notable differences in the relative stability of (*hkl*) facets when the pH conditions change (Figure 5).

In detail, the (001) surface shows a major decrease in cleavage energy from ~ 870 to ~ 250 mJ/m^2 after protonation to monohydrogen phosphate in the top layer. Further

protonation to dihydrogen phosphate hardly affected cleavage further, arriving at ~ 220 mJ/m^2 . The monohydroxylated (010) surface exhibits only a moderate decrease from ~ 1080 to 640 mJ/m^2 after formation of monohydrogen phosphate, related to removal of fewer calcium ions per surface area, a slightly higher negative charge on monohydrogen phosphate (Table 3) and uneven geometry (Figure 5). The second protonation step lowers the surface energy to ~ 320 mJ/m^2 . The (020) surface also exhibits stepwise decreases in cleavage energy from ~ 1220 to ~ 400 mJ/m^2 and to ~ 255 mJ/m^2 . The (101) surface showed stepwise decreases to ~ 390 and ~ 245 mJ/m^2 upon protonation to $\text{pH} \sim 10$ and $\text{pH} \sim 5$, respectively (Table 6). As a result, the (001) surface is of distinctly lower energy than the other surfaces at intermediate protonation to monohydrogen phosphate. At the stage of dihydroxylated surfaces, all four chosen surfaces are of similar cleavage energy within ± 50 mJ/m^2 (Table 6). Similar compositions on every facet, less calcium ions per surface area and dominance of dihydrogen phosphate increase the structural similarity at $\text{pH} \sim 5$ (Figure 3). Also more degrees of freedom such as translation and rotation of dihydrogen phosphate ions are observed. It is also noted that, especially for the (010) surface, water penetration and

protonation into more than the topmost molecular layer would likely decrease the reported cleavage energies further. Therefore, the given values are a first guide and upper limit.

Quantitative experimental data are scarce due to the difficulty to control surface protonation and hydration for a given number of subsurface layers (see details in section S3.4 in the Supporting Information). Slow cleavage of structurally similar fluoroapatite⁹⁵ in air lead to estimates of 95 ± 25 mJ/m² on (001) surfaces and 480 ± 30 mJ/m² on (010) surfaces.¹¹⁶ The result for the (010) plane is in the same range as computed values for partly protonated surfaces (Table 6). Large differences between the computed and measured cleavage energies for the basal (001) plane may be associated with difficulties in humidity control during the measurement.^{116,117} More evidence for the computed facet-averaged cleavage energies of monohydrogen phosphate and dihydrogen phosphate terminated HAP can be derived by comparison to available measurements for C–S–H (Ca₃Si₂O₇·2H₂O) and selenite (CaSO₄·2H₂O) of 386 and 352 mJ/m².^{118,119} These compounds reflect left (Si) and right (S) neighbors to Ca phosphates (P) in the periodic table, are of similar polarity, and contain some crystal water to reflect initial hydration or protonation, respectively. The surface energies in the range 300 to 400 mJ/m² are similar to the surface energy of hydroxyapatite at pH ~ 7 (between monohydrogen phosphate and dihydrogen phosphate termination). Future studies may also reveal more details of the impact of water penetration and protonation deeper than 0.5 nm on cleavage and cohesive properties.

7. INTERACTION OF HYDROXYAPATITE SURFACES WITH WATER AND THE STRUCTURE OF SOLID–LIQUID INTERFACES

The enthalpy of immersion and structure of the solid–liquid interfaces was examined for the same Miller planes (Figure 6 and Table 7). Freshly cleaved, chemically unmodified hydroxyapatite surfaces maintain a distinct boundary with the liquid phase (Figure 6, left column) which becomes increasingly disordered and diffuse upon protonation (Figure 6, center and right columns). The simulations at different pH values show that dissolution processes can be visualized in a simulation. As the pH value decreases, the hydration energy is reduced for all facets similar to the cleavage energy. Reduced hydration energies at lower pH values correlate with leaching of hydroxide ions, reduced area density of calcium ions on the surfaces, and decreased atomic charges on the oxygen atoms of monohydrogen phosphate and dihydrogen phosphate ions in comparison to phosphate ions (Figure 1 and Table 3).

7.1. Immersion Energy. Immersion energies for the different facets provide a quantitative measure for the affinity of hydroxyapatite toward water and enable comparisons to experimental data from calorimetry and adsorption isotherms (Table 7).^{61,120,121} Computed values of the energy of immersion range from 520 to 800 mJ/m² for the surfaces at pH 10 and from 360 to 620 mJ/m² for the same surfaces at pH 5 depending on facet. Values at the high end are seen for (010) facets, related to hydration and protonation of only the topmost phosphate layer on this corrugated surface. The characteristic roughness of the (010) surface can be relieved by reconstruction to a (020) surface upon hydration and partial dissolution. Typical values for protonation of the entire exposed surface are in the range 500 to 670 mJ/m² at pH 10 and 350 to 500 mJ/m² at pH 5, respectively. The energy of immersion

Table 7. Energy of Immersion of Hydroxyapatite Surfaces According to Simulation and Experimental Data (in mJ/m²)^a

method	immersion energy (mJ/m ²)			
	(001)	(010)	(020)	(101)
1. computed at pH ~ 10, HPO₄⁻ terminated				
9-6 LJ ^b	509	753	518	649
12-6 LJ ^b	530	820	572	683
facet average ^c	734; 629 (equal weight)			
2. computed at pH ~5, H₂PO₄⁻ terminated				
9-6 LJ ^b	354	612	476 ^d	481 ^d
12-6 LJ ^b	367	631	509 ^d	492 ^d
facet average ^c	567; 490 (equal weight)			
experimental data (pH ~7)				
adsorption isotherm of water (precipitated and dry samples) ^e	365.3, 432.5, 476.3 (20 °C, facet-average)			
	234.5, 373.5, 407.3 (25 °C, facet-average)			
calorimetry (dry/hot samples) ^f	~600 (25 °C, facet-average)			
calorimetry (dry/hot samples) ^g	~700 (25 °C, facet-average)			

^aEnergy expressions with a 12-6 LJ potential yield immersion energies that on average 2–10% higher than the energy expressions with a 9-6 LJ potential. ^bThe numerical uncertainty of simulated immersion energies is $\pm 2\%$ for each value, corresponding to ± 10 to ± 15 mJ/m². The total uncertainty can reach up to $\pm 5\%$ according to the maximum spread between 12 and 6 and 9-6 values. ^cThe dominant (010) surface is assumed to contribute 70% and the remaining facets 10% each. Alternatively, equal contributions of 25% of each facet are assumed to the total immersion energy. ^dSome dihydrogen phosphate ions begin to dissolve during the simulation. ^eReference 120. Free energies of immersion are reported here and the corresponding energies of immersion can be obtained by addition of +40 mJ/m², i.e., up to 156 mJ/m² (see text). ^fReference 61. ^gReference 121.

would likely decrease also further when initial hydration and protonation extend beyond the topmost molecular layer, as assumed in this study, to include additional subsurface layers.

7.2. Comparison to Measurements. Available measurements of immersion energies and immersion free energies range from 234 to 700 mJ/m², generally in the same range as the simulation (Table 7).^{61,120,121} Experiments were performed on polycrystalline (pellet-pressed) substrates near neutral pH, however. Polycrystalline samples have no defined facet composition and sample preparation differs from one study to another. Several samples were prepared by precipitation from hot solution and resulted in low immersion free energies (234 to 432 mJ/m²).¹²⁰ The surfaces in these studies were already hydrated before the measurement, related to the high affinity of Ca²⁺ ions to water, and reported immersion energies of HAP are therefore too low. One set of samples was prepared by solid state reaction at 1200 °C and resulted in an immersion free energy up to 476 mJ/m².¹²⁰ Even in this case, superficial hydration in air prior to measurement was still possible. The immersion energy of perfectly dry HAP crystals was determined to be 600 to 700 mJ/m² by calorimetry as a function of increasing temperature before dehydration and introduction of P–O–P bonds occurred.^{61,121} The calorimetric data appear most reliable and compare well with simulation results. To compute a facet-average immersion energy from MD simulation, the immersion energies for various (*hkl*) facets can be weighted according to their contribution to the overall nanocrystal shape (Figure 2). Data by Tanaka⁶¹ also specify the ratio of HPO₄²⁻ and H₂PO₄⁻ on HAP surfaces as 31:69 at

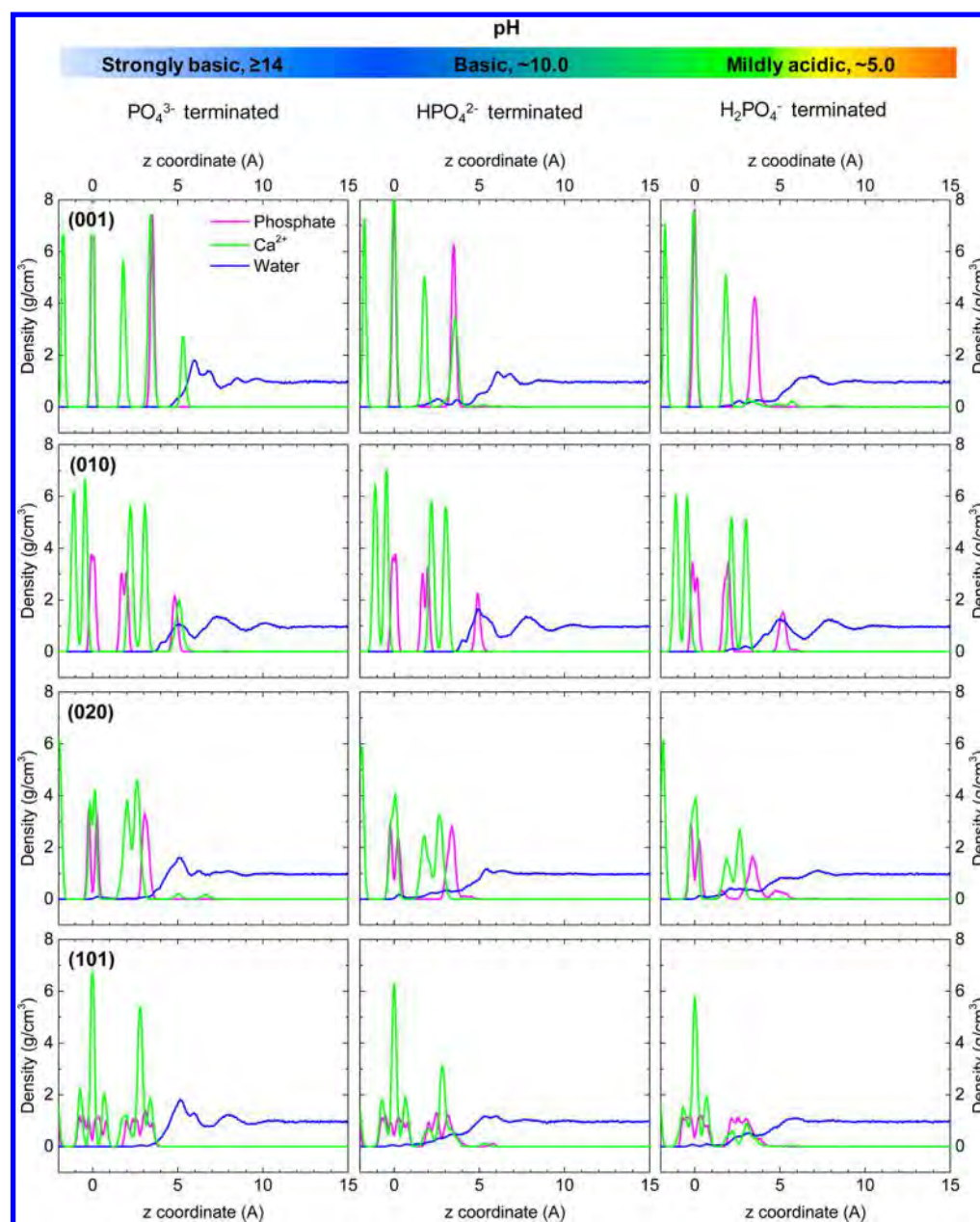


Figure 7. Density profiles of phosphate ions, calcium ions, and water at the (001), (010), (020), and (101) hydroxyapatite surfaces at different pH values, assuming hydration of the top molecular layer on the surface. The density profile of phosphate including all protonated phosphate species at the surface, calcium, and water differs from facet to facet. The loss of superficial calcium ions can be seen on all facets upon decreasing pH value. Less reconstruction is observed on phosphate-terminated surfaces at high pH values in comparison to monohydrogen phosphate-terminated surfaces and dihydrogen phosphate-terminated surfaces at low pH values, particularly on the (020) and the (101) planes. The water density profiles indicate layering and short-range order near the surfaces. At low pH, water density fluctuations near the surface are reduced and penetration into subsurface layers occurs.

neutral pH near 7. If equal weight of the four facets is assumed, the computed facet-average immersion energy at pH 7 is $629 \times 0.31 + 490 \times 0.69 = 533 \text{ mJ/m}^2$ (Table 7). More realistically, data from crystal growth and computed immersion energies indicate that the (010) facet is dominant (Figure 2). The computed facet-average immersion energy at neutral pH then amounts to 619 mJ/m^2 , assuming a contribution of the (010) facets of 70% and of each remaining facet of 10%. This shape-average immersion energy correlates well with the calorimetry measurements in the range of $600\text{--}700 \text{ mJ/m}^2$.

The experimental data for comparison include calorimetrically measured energies of hydration, $\Delta E_{\text{hyd}} (= -\Delta E_{\text{imm}})$ as well

as free energies of hydration obtained from adsorption isotherms, $\Delta A_{\text{hyd}} = \Delta E_{\text{hyd}} - T\Delta S_{\text{hyd}}$, which include changes in entropy upon adsorption of water. As a result of reduced water mobility on the surface, the energy of immersion is 30 to 50 mJ/m^2 higher than the free energy of immersion (note that the energy and free energy of immersion are conventionally stated with a positive sign even though immersion is an exothermic process; see details in section S4.1 in the Supporting Information). Accordingly, the free energy of immersion of 476 mJ/m^2 based on adsorption isotherms (Table 7) corresponds to an energy of immersion of $\sim 516 \text{ mJ/m}^2$. The overall correlation between simulation ($\sim 620 \text{ mJ/m}^2$)

and experiment (520 to 700 mJ/m²) for the facet averaged energies of immersion is therefore very good.

7.3. Facet-Specific Trends. A benefit of the computational models is insight into hydration properties as a function of pH and (*hkl*) crystal facet, which has not (yet) been accessible by experiment. The results show that the (010) surface is the most attractive surface for water in a pH range from 10 to 5, corresponding to an immersion energy of ~790 to ~620 mJ/m², respectively (Figure 6). The high affinity of the prismatic (010) plane to water correlates with its dominance of the surface area of hexagonal, rod-like HAP crystals (Figure 2).^{122–124} The surface with the least affinity to water is the (001) surface, also across a pH range from 10 to 5, corresponding to an immersion energy of ~520 to ~360 mJ/m², respectively (Figure 6). In agreement, the (001) basal plane is known to cover less surface area and is the fastest-growing plane on hexagonal HAP crystallites.^{122–124} These facet-specific differences suggest correlations between the affinity toward water and preferred nanocrystal shape.

Hydration energies of apatite surfaces therefore depend on pH, crystal facet, as well as on the initial depth of water penetration and protonation. Further detailed studies using the atomistic models may elucidate the relative stability of facets and apatite nanocrystals of different shape under various conditions.

Moreover, computed immersion energies using an energy expression with a 12-6 Lennard-Jones potential, e.g. CHARMM, AMBER, tend to be 2% to 10% percent higher than using a 9-6 potential, e.g. PCFF, when all other parameters remain the same (Table 7). This difference is associated with the energy expression and smaller than the experimental uncertainty. Figure 6 reports averages of the two energies.

The relative stability of facets could also be evaluated by solid–liquid interfacial tensions ($\gamma_{\text{SL}} = \Delta A_{\text{Hydr}} + \gamma_{\text{SV}} + \gamma_{\text{LV}}$). The difficulty for reconstructing and dynamic surfaces is, however, that the surface free energy $\gamma_{\text{SV}} \approx E_{\text{Cleav}}$ the hydration energy $\Delta A_{\text{Hydr}} \approx -E_{\text{Imm}}$, and the interfacial tension γ_{SL} become a function of the initial depth of water penetration and protonation in addition to pH and (*hkl*) crystal facet. Estimates of γ_{SL} using available data from Figures 5 and 6 and the water surface tension ($\gamma_{\text{LV}} = 72 \text{ mJ/m}^2$) indicate slightly negative values, suggesting a trend toward dissolution and further hydration of subsurface layers.

7.4. Density Profiles of Phosphate Ions, Calcium Ions, and Water. Density profiles of the hydroxyapatite–water interfaces reveal specific details for each facet at different pH values (Figure 7). A unique facet-specific spacing of phosphate and calcium ions can be seen. The variation in sequence and distance of these ions at the surface is a major reason for the variation in the adsorption of water (Table 7), as well as for the variation in the adsorption of biological and organic molecules. The second or third subsurface average atomic positions of phosphorus were chosen as a reference coordinate of 0 Å in Figure 7. In the present models, hydration and protonation was restricted to the topmost layer of phosphate ions, i.e., about 5 Å depth.

The density profiles visualize the loss of calcium at the surface with decreasing pH for all four facets, leading to a lower Ca:P ratio as observed in NMR measurements.^{53–56} This is a result of the progressive hydration and dissolution of calcium hydroxide from pH >14 toward pH ~5, which leads to dissolution of much of the Ca²⁺ content at the aqueous interfaces (Figure 1). In the same sequence toward lower pH,

decreasing local maxima in phosphate density on all facets indicate a reduced definition of the outer phosphate atomic positions near the solid–liquid interface (Figure 7). The broadening of superficial phosphate positions is associated with a randomization of its orientation on the surface. At the aqueous interface of (020) and (101) facets at pH values of 10 to 5, even partial dissolution of HPO₄²⁻ ions and H₂PO₄⁻ ions is observed while (001) and (010) facets exhibit more resistance to phosphate dissociation. These observations are consistent with experimental observations of higher solubility of dihydrogen phosphate in water compared to monohydrogen phosphate.⁶² We note that the observation of ion dissolution at the surface does not affect the structural stability of the neat mineral a few atomic layers below (stable over 100+ ns duration in the simulation).

The density profiles of superficial water exhibit visible layering at higher pH, related to higher surface charge and cation density of apatite (Figure 7). Close to the outer layer of calcium ions and phosphate ions on the hydroxyapatite surface, two to four recognizable water layers are seen that converge to the bulk density of water at about 5 to 10 Å distance. The first layer sometimes features two separate peaks, for example, on (001) and (101) surfaces, that are related to the surface corrugation of alternating phosphate and calcium ions by about 1 Å (Figure 6). Lower pH values reduce the definition of distinct water layers, except on the strongly corrugated (010) surface. The observations of interfacial layering of water are similar to those reported for other oxide surfaces.⁶⁸ Moreover, water penetration up to about 5 Å into the subsurface layers of Ca²⁺ and phosphate is observed on all facets at lower pH values (see highlights in Figure 6 and density profiles in Figure 7). Lower surface charge and accompanying surface disorder at lower pH smoothen the water density profile and ease the penetration of water into the mineral.

It appears likely that water penetration as well as partial dissolution of hydrogen phosphate ions would extend deeper into the surface once more surface layers participate in the hydration reaction. The level of penetration may be controlled by moisture level, temperature, and exposure time in experiment, and can be represented by the depth of Ca(OH)₂ leaching and phosphate protonation in the models. Details remain to be explored in future studies by appropriately constructed atomistic models and experimental measurements.

7.5. Biomolecule Adsorption. The adsorption of peptides, DNA, and other polymers to various apatite surfaces can be studied in aqueous solution using the proposed force fields (e.g., CHARMM-INTERFACE) and surface models, similar as previously described for silica and other minerals.^{42,43,90,125} A proof-of-concept example is shown here for the conformation of a HAP-binding peptide identified by phage display, S(+)\VSVGK(+)(-)\Cl(-),^{31,66} on the (001) basal plane of the mineral as a function of pH (Figure 8). Multiple independent start structures were subjected to molecular dynamics simulations at pH 10 and 5. Simulation times of ~20 ns at 298 K, combined with annealing^{42,45,71} and REST simulations,^{126,127} achieved good convergence in energies ($\pm 1 \text{ kcal/mol}$) and peptide conformations. Advanced techniques for conformation sampling were not strictly required since the peptide molecule is short and binding energies only slightly negative (see details in section S5.8 in the Supporting Information)."

At pH 10, negatively charged carboxylate groups in the peptide interact with calcium ions on the surface, and

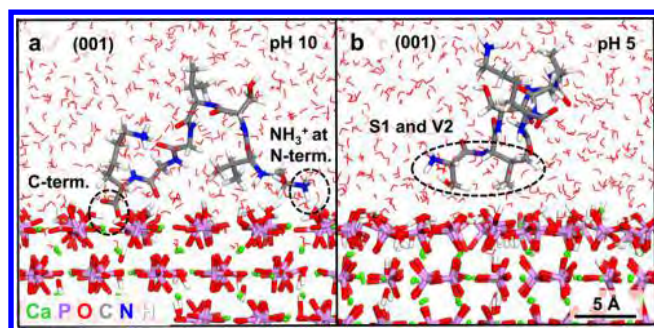


Figure 8. Adsorption of peptide SVSVGK on the hydroxyapatite basal plane (001). Representative conformations and binding groups change significantly for pH values of 10 versus 5 (see black dashed highlights). (a) Ionic groups are attracted to the surface at pH 10. (b) Hydrophobic/polar groups are attracted to the surface at pH 5.

ammonium groups at the N-terminal end are in close contact with hydrogen phosphate ions on the surface (Figure 8a). Ion pairing and ion exchange are dominant contributions to adsorption. At pH 5, different residues such as serine (S1) and valine (V2) are attracted to the apatite surface, related to the lower area density of cations (Figure 8b). Binding is then mostly mediated by hydrogen bonds and hydrophobic interactions.^{41,42} A detailed discussion of selective adsorption as a function of biopolymer sequence, facet, and pH will be reported separately (see preview in refs 67 and 40).

8. CONCLUSIONS

Force field parameters and surface models of hydroxyapatite were introduced and extensively tested for a range of different facets and pH values in aqueous environment. The force field parameters are compatible with numerous harmonic energy expressions, including PCFF, COMPASS, CHARMM, DREIDING, GROMACS, AMBER, CVFF, and OPLS-AA. The parameters are also part of the INTERFACE force field that includes accurate parameters for other minerals and metals.⁷⁴ The new parameters and models facilitate molecular dynamics and Monte Carlo simulations of aqueous, organic, and biomolecular interfaces of apatites under realistic solution conditions including pH and ionic strength, which is a major improvement over earlier models. The force field for hydroxyapatite is developed in the INTERFACE context to add to a uniform force field for all types of compounds across the periodic table that verifies thermodynamic consistency for each compound and uses standard combination rules for nonbond parameters. It reproduces atomic scale as well as bulk properties in excellent agreement with laboratory measurements, including atomic charges, van-der-Waals radii, bonded parameters, lattice parameters, cleavage energies, hydration energies, and elastic constants. Computed lattice parameters deviate less than 0.5% from XRD data on average, the cleavage energy of HAP surfaces agrees with that of chemically similar compounds, computed elastic constants are of the same accuracy as results from quantum mechanical calculations (deviation of ~10% from measurements), and the computed IR spectrum approximates experimentally measured frequencies of O–P–O bending, P–O stretching, and O–H stretching vibrations well.

A suite of atomistic models for hydrated and protonated hydroxyapatite surfaces is introduced that covers (h k l) facets over a range of pH values using extensive experimental data on acid–base equilibria and surface spectroscopy. Hydration

energies are found to be facet-specific and diminish toward lower pH, accompanied by an increase in surface disorder and partial dissolution. These trends correlate with a decrease in the area density of ionic groups on the (h k l) facets. Computed hydration energies are in good agreement with facet-average experimental measurements at pH ~ 7. The models for apatite surfaces can be adjusted to different degrees of hydration, protonation, and surface penetration. Defects such as carbonate ions, magnesium ions, and fluoride ions can also be incorporated exploiting the coverage of the PCFF-INTERFACE, CHARMM-INTERFACE, and other energy expressions for such ions. First examples of highly specific binding of peptides also demonstrate the applicability of the force field to biological interfaces.

The force field and the surface model database provide a new computational tool to explore mechanisms of specific recognition and assembly of apatite-biological interfaces on the 1 to 100 nm scale in comparison with laboratory and clinical studies. Applications are envisioned toward understanding the structure of bone and teeth, osteoporosis and bone implants, caries and dental ceramics, protein-driven apatite mineralization and demineralization, drug screening on apatite surfaces, as well as calcification in arteries. Moreover, biomechanics of protein–apatite composites could be studied in high accuracy at length and time scales a million times larger than those accessible by quantum mechanical methods. Realistic models and simulations of apatites have the potential to contribute toward solutions of grand medical challenges. The aim of this work is to provide sufficient detail and initial validation to open up such exciting research opportunities.

■ ASSOCIATED CONTENT

Supporting Information

The Supporting Information is available free of charge on the ACS Publications website at DOI: 10.1021/acs.jpcc.5b12504.

Details of the prior state of the art, force field, surface models, solid–liquid interfaces, and description of the computational methods. (PDF)

Coordinate files of hydroxyapatite surface models for different facets and pH values in .car/.mdf format including documentation. (ZIP)

■ AUTHOR INFORMATION

Corresponding Author

*E-mail: hendrik.heinz@colorado.edu.

Notes

The authors declare no competing financial interest.

■ ACKNOWLEDGMENTS

The authors acknowledge support by the National Science Foundation (DMR 0955071, DMR 1437355, CBET 1530790), UES, Inc., the Air Force Research Laboratory, Procter and Gamble Co, the Office of Naval Research (ONR-MURI N00014-14-1-0675), the University of Akron, and the University of Colorado Boulder. The allocation of computational resources at the Ohio Supercomputing Center and at the CU Biofrontiers Computing Cluster is acknowledged. This work also utilized the Janus supercomputer, which is supported by the National Science Foundation (Award No. CNS-0821794) and the University of Colorado Boulder.

REFERENCES

- (1) Lowenstam, H. A.; Weiner, S. *On Biomineralization*; Oxford University Press: New York, 1989.
- (2) Mann, S. *Biomineralization Principles and Concepts in Bioinorganic Materials Chemistry*; Oxford University Press: New York, 2001.
- (3) Mann, S. Molecular Recognition in Biomineralization. *Nature* **1988**, *332*, 119–124.
- (4) Mann, S. Molecular Tectonics in Biomineralization and Biomimetic Materials Chemistry. *Nature* **1993**, *365*, 499–505.
- (5) Connett, P.; Follmann, H.; Lammers, M.; Mann, S.; Odom, J.; Wetterhahn, K.; Mann, S. *Inorganic Elements in Biochemistry*; Springer: Berlin, 1983; Vol. 54, pp 125–174.
- (6) Mann, S. On the Nature of Boundary-Organized Biomineralization (BOB). *J. Inorg. Biochem.* **1986**, *28*, 363–371.
- (7) Simmer, J. P.; Fincham, A. G. Molecular Mechanisms of Dental Enamel Formation. *Crit. Rev. Oral Biol. Med.* **1995**, *6*, 84–108.
- (8) Doi, Y.; Eanes, E. D.; Shimokawa, H.; Termine, J. D. Inhibition of Seeded Growth of Enamel Apatite Crystals by Amelogenin and Enamelin Proteins in vitro. *J. Dent. Res.* **1984**, *63*, 98–105.
- (9) Addadi, L.; Weiner, S. Interactions Between Acidic Proteins and Crystals: Stereochemical Requirements in Biomineralization. *Proc. Natl. Acad. Sci. U. S. A.* **1985**, *82*, 4110–4114.
- (10) Gajjaraman, S.; Narayanan, K.; Hao, J.; Qin, C.; George, A. Matrix Macromolecules in Hard Tissues Control the Nucleation and Hierarchical Assembly of Hydroxyapatite. *J. Biol. Chem.* **2007**, *282*, 1193–1204.
- (11) Vallet-Regí, M.; González-Calbet, J. M. Calcium Phosphates as Substitution of Bone Tissues. *Prog. Solid State Chem.* **2004**, *32*, 1–31.
- (12) Dorozhkin, S. Calcium Orthophosphates. *J. Mater. Sci.* **2007**, *42*, 1061–1095.
- (13) Dorozhkin, S. V. Nanosized and Nanocrystalline Calcium Orthophosphates. *Acta Biomater.* **2010**, *6*, 715–734.
- (14) Dorozhkin, S. V.; Dorozhkina, E. I.; Epple, M. A Model System to Provide a Good in Vitro Simulation of Biological Mineralization. *Cryst. Growth Des.* **2004**, *4*, 389–395.
- (15) Misra, D. N.; Bowen, R. L.; Mattamal, G. J. Surface-Area of Dental Enamel, Bone, and Hydroxyapatite - Chemisorption from Solution. *Calcif. Tissue Res.* **1978**, *26*, 139–142.
- (16) Rakovan, J. Growth and Surface Properties of Apatite. *Rev. Mineral. Geochem.* **2002**, *48*, 51–86.
- (17) Rubin, M. A.; Jasiuk, I.; Taylor, J.; Rubin, J.; Ganey, T.; Apkarian, R. P. TEM Analysis of the Nanostructure of Normal and Osteoporotic Human Trabecular Bone. *Bone* **2003**, *33*, 270–282.
- (18) Bilezikian, J. P.; Raisz, L. G.; Martin, T. J. *Principles of Bone Biology*, 3rd ed.; Elsevier Science: London, 2008.
- (19) George, A.; Veis, A. Phosphorylated Proteins and Control over Apatite Nucleation, Crystal Growth, and Inhibition. *Chem. Rev.* **2008**, *108*, 4670–4693.
- (20) Dey, A.; Bomans, P. H. H.; Muller, F. A.; Will, J.; Frederik, P. M.; de With, G.; Sommerdijk, N. The Role of Prenucleation Clusters in Surface-Induced Calcium Phosphate Crystallization. *Nat. Mater.* **2010**, *9*, 1010–1014.
- (21) Nudelman, F.; Pieterse, K.; George, A.; Bomans, P. H. H.; Friedrich, H.; Brylka, L. J.; Hilbers, P. A. J.; de With, G.; Sommerdijk, N. The Role of Collagen in Bone Apatite Formation in the Presence of Hydroxyapatite Nucleation Inhibitors. *Nat. Mater.* **2010**, *9*, 1004–1009.
- (22) Wang, D. A.; Varghese, S.; Sharma, B.; Strehin, I.; Fermanian, S.; Gorham, J.; Fairbrother, D. H.; Cascio, B.; Elisseeff, J. H. Multifunctional Chondroitin Sulphate for Cartilage Tissue-Biomaterial Integration. *Nat. Mater.* **2007**, *6*, 385–392.
- (23) Wang, J.; Yang, M.; Zhu, Y.; Wang, L.; Tomsia, A. P.; Mao, C. Phage Nanofibers Induce Vascularized Osteogenesis in 3D Printed Bone Scaffolds. *Adv. Mater.* **2014**, *26*, 4961–4966.
- (24) Rey, C.; Combes, C.; Drouet, C.; Sfihi, H.; Barroug, A. Physico-Chemical Properties of Nanocrystalline Apatites: Implications for Biominerals and Biomaterials. *Mater. Sci. Eng., C* **2007**, *27*, 198–205.
- (25) Russell, R. G. G.; Watts, N. B.; Ebetino, F. H.; Rogers, M. J. Mechanisms of Action of Bisphosphonates: Similarities and Differences and Their Potential Influence on Clinical Efficacy. *Osteoporosis Int.* **2008**, *19*, 733–759.
- (26) Nancollas, G. H.; Tang, R.; Phipps, R. J.; Henneman, Z.; Gulde, S.; Wu, W.; Mangood, A.; Russell, R. G. G.; Ebetino, F. H. Novel Insights into Actions of Bisphosphonates on Bone: Differences in Interactions with Hydroxyapatite. *Bone* **2006**, *38*, 617–627.
- (27) Corno, M.; Rimola, A.; Bolis, V.; Ugliengo, P. Hydroxyapatite as a Key Biomaterial: Quantum-Mechanical Simulation of its Surfaces in Interaction with Biomolecules. *Phys. Chem. Chem. Phys.* **2010**, *12*, 6309–6329.
- (28) Lawson, M. A.; Xia, Z.; Barnett, B. L.; Triffitt, J. T.; Phipps, R. J.; Dunford, J. E.; Locklin, R. M.; Ebetino, F. H.; Russell, R. G. G. Differences Between Bisphosphonates in Binding Affinities for Hydroxyapatite. *J. Biomed. Mater. Res., Part B* **2010**, *92B*, 149–155.
- (29) Yang, Y.; Cui, Q.; Sahai, N. How Does Bone Sialoprotein Promote the Nucleation of Hydroxyapatite? A Molecular Dynamics Study Using Model Peptides of Different Conformations. *Langmuir* **2010**, *26*, 9848–9859.
- (30) Friddle, R. W.; Battle, K.; Trubetsky, V.; Tao, J.; Salter, E. A.; Moradian-Oldak, J.; De Yoreo, J. J.; Wierzbicki, A. Single-Molecule Determination of the Face-Specific Adsorption of Amelogenin's C-Terminus on Hydroxyapatite. *Angew. Chem., Int. Ed.* **2011**, *50*, 7541–7545.
- (31) Weiger, M. C.; Park, J. J.; Roy, M. D.; Stafford, C. M.; Karim, A.; Becker, M. L. Quantification of the Binding Affinity of a Specific Hydroxyapatite Binding Peptide. *Biomaterials* **2010**, *31*, 2955–2963.
- (32) Segvich, S. J.; Smith, H. C.; Kohn, D. H. The Adsorption of Preferential Binding Peptides to Apatite-Based Materials. *Biomaterials* **2009**, *30*, 1287–1298.
- (33) Harding, I. S.; Rashid, N.; Hing, K. A. Surface Charge and the Effect of Excess Calcium Ions on the Hydroxyapatite Surface. *Biomaterials* **2005**, *26*, 6818–6826.
- (34) Heinz, H.; Ramezani-Dakhel, H. Simulations of Inorganic–Bioorganic Interfaces to Discover New Materials: Insights, Comparisons to Experiment, Challenges, and Opportunities. *Chem. Soc. Rev.* **2016**, *45*, 412–448.
- (35) Kirkham, J.; Brookes, S. J.; Shore, R. C.; Wood, S. R.; Smith, D. A.; Zhang, J.; Chen, H.; Robinson, C. Physico-Chemical Properties of Crystal Surfaces in Matrix-Mineral Interactions during Mammalian Biomineralisation. *Curr. Opin. Colloid Interface Sci.* **2002**, *7*, 124–132.
- (36) Flade, K.; Lau, C.; Mertig, M.; Pompe, W. Osteocalcin-Controlled Dissolution–Reprecipitation of Calcium Phosphate under Biomimetic Conditions. *Chem. Mater.* **2001**, *13*, 3596–3602.
- (37) Johnsson, M.; Levine, M. J.; Nancollas, G. H. Hydroxyapatite Binding Domains in Salivary Proteins. *Crit. Rev. Oral Biol. Med.* **1993**, *4*, 371–378.
- (38) Kirkham, J.; Zhang, J.; Brookes, S. J.; Shore, R. C.; Wood, S. R.; Smith, D. A.; Wallwork, M. L.; Ryu, O. H.; Robinson, C. Evidence for Charge Domains on Developing Enamel Crystal Surfaces. *J. Dent. Res.* **2000**, *79*, 1943–1947.
- (39) Wallwork, M. L.; Kirkham, J.; Zhang, J.; Smith, D. A.; Brookes, S. J.; Shore, R. C.; Wood, S. R.; Ryu, O.; Robinson, C. Binding of Matrix Proteins to Developing Enamel Crystals: An Atomic Force Microscopy Study. *Langmuir* **2001**, *17*, 2508–2513.
- (40) Heinz, H. The Role of Chemistry and pH of Solid Surfaces for Specific Adsorption of Biomolecules in Solution—Accurate Computational Models and Experiment. *J. Phys.: Condens. Matter* **2014**, *26*, 244105.
- (41) Patwardhan, S. V.; Emami, F. S.; Berry, R. J.; Jones, S. E.; Naik, R. R.; Deschaume, O.; Heinz, H.; Perry, C. C. Chemistry of Aqueous Silica Nanoparticle Surfaces and the Mechanism of Selective Peptide Adsorption. *J. Am. Chem. Soc.* **2012**, *134*, 6244–6256.
- (42) Emami, F. S.; Puddu, V.; Berry, R. J.; Varshney, V.; Patwardhan, S. V.; Perry, C. C.; Heinz, H. Prediction of Specific Biomolecule Adsorption on Silica Surfaces as a Function of pH and Particle Size. *Chem. Mater.* **2014**, *26*, 5725–5734.
- (43) Mishra, R. K.; Flatt, R. J.; Heinz, H. Force Field for Tricalcium Silicate and Insight into Nanoscale Properties: Cleavage, Initial

Hydration, and Adsorption of Organic Molecules. *J. Phys. Chem. C* **2013**, *117*, 10417–10432.

(44) Heinz, H.; Suter, U. W. Surface Structure of Organoclay. *Angew. Chem., Int. Ed.* **2004**, *43*, 2239–2243.

(45) Ramezani-Dakhel, H.; Ruan, L. Y.; Huang, Y.; Heinz, H. Molecular Mechanism of Specific Recognition of Cubic Pt Nanocrystals by Peptides and the Concentration-Dependent Formation from Seed Crystals. *Adv. Funct. Mater.* **2015**, *25*, 1374–1384.

(46) Rootare, H. M.; Craig, R. G. Vapor Phase Adsorption of Water on Hydroxyapatite. *J. Dent. Res.* **1977**, *56*, 1437–1448.

(47) Rootare, H. M.; Deitz, V. R.; Carpenter, F. G. Solubility Product Phenomena in Hydroxyapatite-Water Systems. *J. Colloid Sci.* **1962**, *17*, 179–206.

(48) Bertazzo, S.; Zambuzzi, W. F.; Campos, D. D. P.; Ogeda, T. L.; Ferreira, C. V.; Bertran, C. A. Hydroxyapatite Surface Solubility and Effect on Cell Adhesion. *Colloids Surf., B* **2010**, *78*, 177–184.

(49) Bertran, C. A.; Bertazzo, S.; Faria, L. P. Surface Charge of Hydroxyapatite and Bone Mineral. *Key Eng. Mater.* **2007**, 330–332, 713–716.

(50) Jäger, C.; Welzel, T.; Meyer-Zaika, W.; Epple, M. A Solid-State NMR Investigation of the Structure of Nanocrystalline Hydroxyapatite. *Magn. Reson. Chem.* **2006**, *44*, 573–580.

(51) Mathew, M.; Takagi, S. Structures of Biological Minerals in Dental Research. *J. Res. Natl. Inst. Stand. Technol.* **2011**, *106*, 1035–1044.

(52) Brown, W. E. Octacalcium Phosphate and Hydroxyapatite: Crystal Structure of Octacalcium Phosphate. *Nature* **1962**, *196*, 1048–1050.

(53) Bengtsson, A.; Shchukarev, A.; Persson, P.; Sjöberg, S. A Solubility and Surface Complexation Study of a Non-Stoichiometric Hydroxyapatite. *Geochim. Cosmochim. Acta* **2009**, *73*, 257–267.

(54) Brown, P. W.; Martin, R. I. An Analysis of Hydroxyapatite Surface Layer Formation. *J. Phys. Chem. B* **1999**, *103*, 1671–1675.

(55) Berry, E. E. The Structure and Composition of Some Calcium-Deficient Apatites. *J. Inorg. Nucl. Chem.* **1967**, *29*, 317–327.

(56) Meyer, J. L.; Fowler, B. O. Lattice Defects in Nonstoichiometric Calcium Hydroxylapatites. A Chemical Approach. *Inorg. Chem.* **1982**, *21*, 3029–3035.

(57) Robinson, C.; Connell, S.; Brookes, S. J.; Kirkham, J.; Shore, R. C.; Smith, D. A. M. Surface Chemistry of Enamel Apatite During Maturation in Relation to pH: Implications for Protein Removal and Crystal Growth. *Arch. Oral Biol.* **2005**, *50*, 267–270.

(58) Ishikawa, T.; Wakamura, M.; Kondo, S. Surface Characterization of Calcium Hydroxylapatite by Fourier Transform Infrared Spectroscopy. *Langmuir* **1989**, *5*, 140–144.

(59) Dorozhkin, S. V. Surface Reactions of Apatite Dissolution. *J. Colloid Interface Sci.* **1997**, *191*, 489–497.

(60) Dorozhkin, S. V. Inorganic Chemistry of the Dissolution Phenomenon: The Dissolution Mechanism of Calcium Apatites at the Atomic (Ionic) Level. *Comments Inorg. Chem.* **1999**, *20*, 285–299.

(61) Tanaka, H.; Chikazawa, M.; Kandori, K.; Ishikawa, T. Influence of Thermal Treatment on the Structure of Calcium Hydroxyapatite. *Phys. Chem. Chem. Phys.* **2000**, *2*, 2647–2650.

(62) *CRC Handbook of Chemistry and Physics*, 89th ed.; CRC Press: Boca Raton, FL, 2008.

(63) Stayton, P. S.; Drobny, G. P.; Shaw, W. J.; Long, J. R.; Gilbert, M. Molecular Recognition at the Protein-Hydroxyapatite Interface. *Crit. Rev. Oral Biol. Med.* **2003**, *14*, 370–376.

(64) Shin, H.; Jo, S.; Mikos, A. G. Biomimetic Materials for Tissue Engineering. *Biomaterials* **2003**, *24*, 4353–4364.

(65) Sodek, J.; Ganss, B.; McKee, M. D. Osteopontin. *Crit. Rev. Oral Biol. Med.* **2000**, *11*, 279–303.

(66) Roy, M. D.; Stanley, S. K.; Amis, E. J.; Becker, M. L. Identification of a Highly Specific Hydroxyapatite-binding Peptide using Phage Display. *Adv. Mater.* **2008**, *20*, 1830–1836.

(67) Lin, T. Z. *Force Field Parameters and Atomistic Surface Models for Hydroxyapatite and Analysis of Biomolecular Adsorption at Aqueous Interfaces*; Retrieved from <https://etd.ohiolink.edu>; PhD thesis; University of Akron, 2013.

(68) Emami, F. S.; Puddu, V.; Berry, R. J.; Varshney, V.; Patwardhan, S. V.; Perry, C. C.; Heinz, H. Force Field and a Surface Model Database for Silica to Simulate Interfacial Properties in Atomic Resolution. *Chem. Mater.* **2014**, *26*, 2647–2658.

(69) Feng, J.; Slocik, J. M.; Sarikaya, M.; Naik, R. R.; Farmer, B. L.; Heinz, H. Influence of the Shape of Nanostructured Metal Surfaces on Adsorption of Single Peptide Molecules in Aqueous Solution. *Small* **2012**, *8*, 1049–1059.

(70) Heinz, H.; Farmer, B. L.; Pandey, R. B.; Slocik, J. M.; Patnaik, S. S.; Pachter, R.; Naik, R. R. Nature of Molecular Interactions of Peptides with Gold, Palladium, and Pd-Au Bimetal Surfaces in Aqueous Solution. *J. Am. Chem. Soc.* **2009**, *131*, 9704–9714.

(71) Jha, K. C.; Liu, H.; Bockstaller, M. R.; Heinz, H. Facet Recognition and Molecular Ordering of Ionic Liquids on Metal Surfaces. *J. Phys. Chem. C* **2013**, *117*, 25969–25981.

(72) Mishra, R. K.; Fernández-Carrasco, L.; Flatt, R. J.; Heinz, H. A Force Field for Tricalcium Aluminate to Characterize Surface Properties, Initial Hydration, and Organically Modified Interfaces in Atomic Resolution. *Dalton Trans.* **2014**, 43, 10602–10616.

(73) Ruan, L. Y.; Ramezani-Dakhel, H.; Lee, C.; Li, Y. J.; Duan, X. F.; Heinz, H.; Huang, Y. A Rational Biomimetic Approach to Structure Defect Generation in Colloidal Nanocrystals. *ACS Nano* **2014**, *8*, 6934–6944.

(74) Heinz, H.; Lin, T.-J.; Mishra, R. K.; Emami, F. S. Thermodynamically Consistent Force Fields for the Assembly of Inorganic, Organic, and Biological Nanostructures: The INTERFACE Force Field. *Langmuir* **2013**, *29*, 1754–1765.

(75) Corni, S.; Hnilova, M.; Tamerler, C.; Sarikaya, M. Conformational Behavior of Genetically-Engineered Dodecapeptides as a Determinant of Binding Affinity for Gold. *J. Phys. Chem. C* **2013**, *117*, 16990–17003.

(76) Hoefling, M.; Iori, F.; Corni, S.; Gottschalk, K. E. Interaction of Amino Acids With the Au(111) Surface: Adsorption Free Energies from Molecular Dynamics Simulations. *Langmuir* **2010**, *26*, 8347–8351.

(77) Heinz, H. Adsorption of Biomolecules and Polymers on Silicates, Glasses, and Oxides: Mechanisms, Predictions, and Opportunities by Molecular Simulation. *Curr. Opin. Chem. Eng.* **2016**, *11*, 34–41.

(78) Bedford, N. M.; Ramezani-Dakhel, H.; Slocik, J. M.; Briggs, B. D.; Ren, Y.; Frenkel, A. I.; Petkov, V.; Heinz, H.; Naik, R. R.; Knecht, M. R. Elucidation of Peptide-Directed Palladium Surface Structure for Biologically Tunable Nanocatalysts. *ACS Nano* **2015**, *9*, 5082–5092.

(79) Coppage, R.; Slocik, J. M.; Ramezani-Dakhel, H.; Bedford, N. M.; Heinz, H.; Naik, R. R.; Knecht, M. R. Exploiting Localized Surface Binding Effects to Enhance the Catalytic Reactivity of Peptide-Capped Nanoparticles. *J. Am. Chem. Soc.* **2013**, *135*, 11048–11054.

(80) Robinson, J.; Cukrowski, I.; Marques, H. M. Modelling the Interaction of Several Bisphosphonates with Hydroxyapatite Using the Generalised AMBER Force Field. *J. Mol. Struct.* **2006**, *825*, 134–142.

(81) Mostafa, N. Y.; Brown, P. W. Computer Simulation of Stoichiometric Hydroxyapatite: Structure and Substitutions. *J. Phys. Chem. Solids* **2007**, *68*, 431–437.

(82) Bhowmik, R.; Katti, K. S.; Katti, D. Molecular Dynamics Simulation of Hydroxyapatite-Polyacrylic Acid Interfaces. *Polymer* **2007**, *48*, 664–674.

(83) Cruz, F. J. A. L.; Canongia Lopes, J. N.; Calado, J. C. G.; Minas da Piedade, M. E. A Molecular Dynamics Study of the Thermodynamic Properties of Calcium Apatites. 1. Hexagonal Phases. *J. Phys. Chem. B* **2005**, *109*, 24473–24479.

(84) de Leeuw, N. H. A Computer Modelling Study of the Uptake and Segregation of Fluoride Ions at the Hydrated Hydroxyapatite (0001) Surface: Introducing a Ca₁₀(PO₄)₆(OH)₂ Potential Model. *Phys. Chem. Chem. Phys.* **2004**, *6*, 1860–1866.

(85) Hauptmann, S.; Dufner, H.; Brickmann, J.; Kast, S. M.; Berry, R. S. Potential Energy Function for Apatites. *Phys. Chem. Chem. Phys.* **2003**, *5*, 635–639.

(86) Mkhonto, D.; de Leeuw, N. H. A Computer Modelling Study of the Effect of Water on the Surface Structure and Morphology of

Fluorapatite: Introducing a Ca₁₀(PO₄)₆F₂ Potential Model. *J. Mater. Chem.* **2002**, *12*, 2633–2642.

(87) Chen, C.; Xia, M.; Wu, L.; Zhou, C.; Wang, F. Modeling the Interaction of Seven Bisphosphonates with the Hydroxyapatite(100) Face. *J. Mol. Model.* **2012**, *18*, 4007–4012.

(88) Pradip; Rai, B.; Rao, T. K.; Krishnamurthy, S.; Vetrivel, R.; Mielczarski, J.; Cases, J. M. Molecular Modeling of Interactions of Alkyl Hydroxamates with Calcium Minerals. *J. Colloid Interface Sci.* **2002**, *256*, 106–113.

(89) Heinz, H.; Suter, U. W. Atomic Charges for Classical Simulations of Polar Systems. *J. Phys. Chem. B* **2004**, *108*, 18341–18352.

(90) Heinz, H.; Koerner, H.; Anderson, K. L.; Vaia, R. A.; Farmer, B. L. Force Field for Mica-Type Silicates and Dynamics of Octadecylammonium Chains Grafted to Montmorillonite. *Chem. Mater.* **2005**, *17*, 5658–5669.

(91) Heinz, H.; Vaia, R. A.; Farmer, B. L.; Naik, R. R. Accurate Simulation of Surfaces and Interfaces of Face-Centered Cubic Metals Using 12–6 and 9–6 Lennard-Jones Potentials. *J. Phys. Chem. C* **2008**, *112*, 17281–17290.

(92) Thong, N.; Schwarzenbach, D. The Use of Electric Field Gradient Calculations in Charge Density Refinements. II. Charge Density Refinement of the Low-Quartz Structure of Aluminum Phosphate. *Acta Crystallogr., Sect. A: Cryst. Phys., Diff., Theor. Gen. Crystallogr.* **1979**, *35*, 658–664.

(93) Brunauer, S.; Kanro, D. L.; Weise, C. H. The Surface Energies of Calcium Oxide and Calcium Hydroxide. *Can. J. Chem.* **1956**, *34*, 729–742.

(94) Hughes, J. M.; Cameron, M.; Crowley, K. D. Structural Variations in Natural F, OH, and Cl Apatites. *Am. Mineral.* **1989**, *74*, 870–876.

(95) Hughes, J. M.; Rakovan, J. The Crystal Structure of Apatite, Ca₅(PO₄)₃(F,OH,Cl). *Rev. Mineral. Geochem.* **2002**, *48*, 1–12.

(96) Kay, M. I.; Young, R. A.; Posner, A. S. Crystal Structure of Hydroxyapatite. *Nature* **1964**, *204*, 1050–1052.

(97) Fowler, B. O. Infrared Studies of Apatites. I. Vibrational Assignments for Calcium, Strontium, and Barium Hydroxyapatites Utilizing Isotopic Substitution. *Inorg. Chem.* **1974**, *13*, 194–207.

(98) Koutsopoulos, S. Synthesis and Characterization of Hydroxyapatite Crystals: A Review Study on the Analytical Methods. *J. Biomed. Mater. Res.* **2002**, *62*, 600–612.

(99) Rehman, I.; Bonfield, W. Characterization of Hydroxyapatite and Carbonated Apatite by Photo Acoustic FTIR Spectroscopy. *J. Mater. Sci.: Mater. Med.* **1997**, *8*, 1–4.

(100) Morgan, H.; Wilson, R. M.; Elliott, J. C.; Dowker, S. E. P.; Anderson, P. Preparation and Characterisation of Monoclinic Hydroxyapatite and its Precipitated Carbonate Apatite Intermediate. *Biomaterials* **2000**, *21*, 617–627.

(101) Batsanov, S. S. Van der Waals Radii of Elements. *Inorg. Mater.* **2001**, *37*, 871–885.

(102) Heinz, H.; Vaia, R. A.; Farmer, B. L. Interaction Energy and Surface Reconstruction Between Sheets of Layered Silicates. *J. Chem. Phys.* **2006**, *124*, 224713.

(103) Fu, Y. T.; Heinz, H. Cleavage Energy of Alkylammonium-Modified Montmorillonite and Relation to Exfoliation in Nanocomposites: Influence of Cation Density, Head Group Structure, and Chain Length. *Chem. Mater.* **2010**, *22*, 1595–1605.

(104) Bolt, G. H. Determination of the Charge Density of Silica Sols. *J. Phys. Chem.* **1957**, *61*, 1166–1169.

(105) Zerrouk, R.; Foissy, A.; Mercier, R.; Chevallier, Y.; Morawski, J.-C. Study of Ca²⁺-Induced Silica Coagulation by Small Angle Scattering. *J. Colloid Interface Sci.* **1990**, *139*, 20–29.

(106) House, W. A.; Orr, D. R. Investigation of the pH Dependence of the Kinetics of Quartz Dissolution at 25 °C. *J. Chem. Soc., Faraday Trans.* **1992**, *88*, 233–241.

(107) Ching, W. Y.; Rulis, P.; Misra, A. Ab Initio Elastic Properties and Tensile Strength of Crystalline Hydroxyapatite. *Acta Biomater.* **2009**, *5*, 3067–3075.

(108) Menéndez-Proupin, E.; Cervantes-Rodríguez, S.; Osorio-Pulgar, R.; Franco-Cisterna, M.; Camacho-Montes, H.; Fuentes, M. E. Computer Simulation of Elastic Constants of Hydroxyapatite and Fluorapatite. *J. Mech. Behav. Biomed. Mater.* **2011**, *4*, 1011–1020.

(109) Snyders, R.; Music, D.; Sigumonrong, D.; Schelnberger, B.; Jensen, J.; Schneider, J. M. Experimental and Ab Initio Study of the Mechanical Properties of Hydroxyapatite. *Appl. Phys. Lett.* **2007**, *90*, 193902.

(110) Katz, J. L.; Ukraincik, K. On the Anisotropic Elastic Properties of Hydroxyapatite. *J. Biomechanics* **1971**, *4*, 221–227.

(111) Gilmore, R. S.; Katz, J. L. Elastic Properties of Apatites. *J. Mater. Sci.* **1982**, *17*, 1131–1141.

(112) Yoon, H. S.; Newnham, R. E. Elastic Properties of Fluoroapatite. *Am. Mineral.* **1969**, *54*, 1193–1197.

(113) de Leeuw, N. H.; Bowe, J. R.; Rabone, J. A. L. A Computational Investigation of Stoichiometric and Calcium-Deficient Oxy- and Hydroxy-Apatites. *Faraday Discuss.* **2007**, *134*, 195–214.

(114) Chung, D. H.; Buessem, W. R. The Voigt-Reuss-Hill Approximation and Elastic Moduli of Polycrystalline MgO, CaF₂, beta-ZnS, ZnSe, and CdTe. *J. Appl. Phys.* **1967**, *38*, 2535–2540.

(115) Filgueiras, M. R. T.; Mkhonto, D.; de Leeuw, N. H. Computer Simulations of the Adsorption of Citric Acid at Hydroxyapatite Surfaces. *J. Cryst. Growth* **2006**, *294*, 60–68.

(116) Aning, M.; Welch, D. O.; Royce, B. S. H. The Surface Energy of Fluorapatite. *Phys. Lett. A* **1971**, *37*, 253–254.

(117) Parks, G. A. Surface and Interfacial Free Energies of Quartz. *J. Geophys. Res.* **1984**, *89*, 3997–4008.

(118) Brunauer, S.; Kanro, D. L.; Weise, C. H. The Surface Energy of Tobermorite. *Can. J. Chem.* **1959**, *37*, 714–724.

(119) Oglesby, M. L.; Gutshall, P. L.; Phillips, J. M. Cleavage Surface Energy of Selenite. *Am. Mineral.* **1976**, *61*, 295–298.

(120) Rootare, H. M.; Craig, R. G. Free Surface Energy Change for Water Adsorbed on Hydroxyapatite. *J. Dent. Res.* **1977**, *56*, 744–747.

(121) Barton, S. S.; Harrison, B. H. Surface Properties of Hydroxyapatites. I. Enthalpy of Immersion. *J. Colloid Interface Sci.* **1976**, *55*, 409–414.

(122) Neira, I. S.; Guitián, F.; Taniguchi, T.; Watanabe, T.; Yoshimura, M. Hydrothermal Synthesis of Hydroxyapatite Whiskers with Sharp Faceted Hexagonal Morphology. *J. Mater. Sci.* **2008**, *43*, 2171–2178.

(123) Teshima, K.; Lee, S.; Sakurai, M.; Kameno, Y.; Yubuta, K.; Suzuki, T.; Shishido, T.; Endo, M.; Oishi, S. Well-Formed One-Dimensional Hydroxyapatite Crystals Grown by an Environmentally Friendly Flux Method. *Cryst. Growth Des.* **2009**, *9*, 2937–2940.

(124) Neira, I. S.; Kolen'ko, Y. V.; Lebedev, O. I.; Van Tendeloo, G.; Gupta, H. S.; Guitián, F.; Yoshimura, M. An Effective Morphology Control of Hydroxyapatite Crystals via Hydrothermal Synthesis. *Cryst. Growth Des.* **2009**, *9*, 466–474.

(125) Heinz, H. Clay Minerals for Nanocomposites and Biotechnology: Surface Modification, Dynamics and Responses to Stimuli. *Clay Miner.* **2012**, *47*, 205–230.

(126) Wright, L. B.; Walsh, T. R. Efficient Conformational Sampling of Peptides Adsorbed onto Inorganic Surfaces: Insights from a Quartz Binding Peptide. *Phys. Chem. Chem. Phys.* **2013**, *15*, 4715–4726.

(127) Ostermeir, K.; Zacharias, M. Enhanced Sampling of Peptides and Proteins with a New Biasing Replica Exchange Method. *J. Biomol. Struct. Dyn.* **2013**, *31*, 106–107.

NOTE ADDED AFTER ASAP PUBLICATION

This article was published ASAP on February 26, 2016, with an error in the Abstract and Table of Contents graphics. The corrected version was published ASAP on March 1, 2016.